

The Kovalevskaya Top

Peter H. Richter, Holger R. Dullin, Andreas Wittek

Institut für Theoretische Physik, University of Bremen
Postfach 330 440, D-28334 Bremen, Germany

Publ. Wiss. Film. Techn. Wiss./Naturw. **13** (1997), 33-96.
Film C 1961. Institut für den Wissenschaftlichen Film, Göttingen

Abstract

The film is an attempt to familiarize the viewer with the fascinating complexity of the Kovalevskaya top. The dynamics of this third integrable case of classical rigid body dynamics is presented on several levels of abstraction, starting from real motion of a physical model and an analogous computer simulation of the Kovalevskaya equations of motion. The first abstraction involves the separation of a cyclic angular variable, i. e., the transition to a reduced description, and the introduction of a six-dimensional (γ, l) -phase space with two Casimir constants. In the next step, relative equilibria are used to identify bifurcations between different topological types of three-dimensional energy surfaces. The third level is concerned with the foliation of these energy surfaces by invariant tori, and with the identification of critical tori which mark bifurcations in the type of foliation. The tori are shown in various 3D projections and in homeomorphic deformations of the energy surfaces. The final step in the analysis uses the technique of Poincaré surfaces of section. A comprehensive survey on all possible motions is given in terms of animation series where all Poincaré sections for a given energy are shown in succession.

1 Introduction

The dynamics of a spinning top in a gravitational field is one of the more challenging topics in classical mechanics. Its technical definition is the following. A rigid body is held fixed in one of its points but otherwise free to move under the influence of gravity. The motion has three angular degrees of freedom. It may be described as the continuous change of the relative orientation between a body-fixed Cartesian reference system K' , with axes $(\mathbf{e}_1, \mathbf{e}_2, \mathbf{e}_3)$, and a space-fixed Cartesian system K , with axes $(\mathbf{e}_x, \mathbf{e}_y, \mathbf{e}_z)$. Without restriction of generality we may assume gravity to point along the negative z direction, $\mathbf{g} = -g\mathbf{e}_z$. The system is then symmetric with respect to rotation about the z axis; the corresponding angle φ may be separated, and the rest treated as a two-degree-of-freedom system.

The *full configuration space* is $Q = SO(3)$, i. e., the set of orientation preserving orthogonal transformations in \mathbb{R}^3 . It is a three-dimensional manifold with a non-commutative group structure and a non-trivial topology. A point $\phi \in Q$ may be parametrized by Euler's angles, $\phi = (\varphi, \vartheta, \psi)$, where $\varphi \in S^1$, $\psi \in S^1$, and $0 \leq \vartheta \leq \pi$. This choice of coordinates has singularities at $\vartheta \rightarrow 0$ and π , where the tori of (φ, ψ) coordinates degenerate to circles with coordinates $\varphi + \psi$ and $\varphi - \psi$, respectively. Unfortunately, $SO(3)$ does not admit for a global system of three coordinates that would be free of singularities. The *phase space* $T^*SO(3) = SO(3) \times \mathbb{R}^3$ consists of coordinates ϕ and canonical momenta $\pi = (\pi_\varphi, \pi_\vartheta, \pi_\psi)$ which will be combined as six-dimensional variables $\mathbf{x} \equiv (\phi, \pi)$. The Hamiltonian $\mathcal{H}(\mathbf{x}) = \mathcal{H}(\phi, \pi)$ is a real function on $T^*SO(3)$ which defines the canonical time development. The five-dimensional surfaces of constant energy $\mathcal{H} = h$ will be called *energy surfaces* \mathcal{E}_h .

The *reduced configuration space*, obtained after separation of the cyclic angle φ at constant value of the angular momentum $\pi_\varphi = l$, is a 2-sphere, $Q_l = S^2$. Like in the case of $SO(3)$, there do not exist singularity-free global coordinates on S^2 . Moreover, the sphere does not even carry a group structure. It has therefore become customary to think of S^2 as embedded in \mathbb{R}^3 , with coordinates $\gamma = (\gamma_1, \gamma_2, \gamma_3)$ in the body-fixed frame of reference K' . These three coordinates together with the three components $\mathbf{l} = (l_1, l_2, l_3)$ of the angular momentum provide a convenient description of the *reduced phase space* T^*S^2 as embedded in a space $P_l = \mathbb{R}^3 \times \mathbb{R}^3$, with points $\mathbf{y} \equiv (\gamma, \mathbf{l})$. The number of dimensions of P_l is again six, but it will be shown in Section 2 that by construction of this space, all motion is effectively restricted to four-dimensional subspaces with topology T^*S^2 . Energy surfaces in the (γ, \mathbf{l}) phase space should correspondingly be understood as three-dimensional manifolds \mathcal{E}_{hl} . This corresponds to the fact that the reduced system has only two degrees of freedom.

We only mention the fact that for the purpose of numerical calculations and graphical simulations of the spinning top, it is convenient to use yet another set of variables. As is well known, the universal covering manifold of $SO(3)$ is the 3-sphere S^3 in which each point of $SO(3)$ has two representations (corresponding to two spin states). Considering S^3 as embedded in \mathbb{R}^4 , rotations of the physical configuration space $SO(3)$ may very elegantly be described if \mathbb{R}^4 is equipped with the structure of quaternion multiplication.

The use of this apparatus for practical applications was strongly advocated by Klein and Sommerfeld [17], but these authors did not care to work out a Hamiltonian formulation on that basis. The more recent mathematical development of rigid body theory seems to have neglected this powerful approach. It will be presented in our forthcoming book on spinning tops [26], and though it does not appear on the surface of our film, it dominates the background computations. Its advantage over the (ϕ, π) equations in $T^*SO(3)$ is that it is free of coordinate singularities and of trigonometric functions; compared to the (γ, l) equations in P_l , it has the benefit of including the φ motion.

Before considering the equations of motion in detail, we mention a practical problem. In order to fix a point of a rigid body in space and yet allow for free rotation of the rest of it, some kind of Cardan suspension is usually employed, where all three angles $(\varphi, \vartheta, \psi)$ may vary independently along a complete circle. In the presence of such a frame, the configuration space assumes the topology of a torus T^3 which is fundamentally different from $SO(3)$. It is by no means trivial to recover $SO(3)$ dynamics from T^3 dynamics in the limit where the mass of the frame tends to zero: a system with a massless frame is topologically different from a system with no frame. This difficulty casts some doubt on the very possibility of observing true $SO(3)$ motion in physical reality, except for the special case of an Euler top where the fixed point is the center of mass. In that case, one may think of a free rigid body in an inertial frame of reference; in all other cases, it should be kept in mind that the absence of a suspending frame involves a severe idealization [25].

But even so, the typical motion defined by this setting is highly complicated. In fact, for almost all choices of principal moments of inertia $\Theta_1, \Theta_2, \Theta_3$, relative to the fixed point, and centers of gravity $\mathbf{c} = (c_1, c_2, c_3)$, in the body-fixed system, the motion is non-integrable. There exist only three special cases where each energy surface $\mathcal{E}_h \subset T^*SO(3)$ is foliated by invariant tori T^3 , and each energy surface $\mathcal{E}_{hl} \subset T^*S^2$ by tori T^2 :

1. The *Euler* case of a rigid body fixed in its center of mass so that gravity plays no role, $(c_1, c_2, c_3) = (0, 0, 0)$.
2. The *Lagrange* case of a symmetric heavy rigid body: two moments of inertia are equal, and the center of mass lies on the axis of symmetry, as for $\Theta_1 = \Theta_2$ and $\mathbf{c} = c\mathbf{e}_3$.
3. The *Kovalevskaya* case where two moments of inertia are equal and twice as large as the third, with the center of mass in the plane of the equal moments. By a suitable identification of principal axes this case can always be characterized as $\Theta_1 = \Theta_2 = 2\Theta_3$ and $\mathbf{c} = -c\mathbf{e}_1$.

The discovery of this last integrable case in 1888 was a most remarkable achievement by the Russian mathematician Sonja Kovalevskaya [19, 20]. It brought her immediate fame and earned her the prestigious Prix Bordin of the Paris Academy of Science. She was able to work out the analytic solution of the equations of motion in terms of hyperelliptic functions, but nonetheless it took generations of mathematicians to uncover the full complexity of the different types of motion that the equations contain. To mention only a few, we cite F. Kötter [18], N. E. Zhukovsky [30], G. G. Appelrot [1], M. P. Kharlamov [16],

B. A. Dubrovin [8], E. Horozov *et al.* [14, 15], A. I. Bobenko *et al.* [6], A. T. Fomenko [13], A. A. Oshemkov [23], D. Lewis *et al.* [21], M. Audin [3], and H. R. Dullin *et al.* [9, 10].

With suitable scaling of the physical quantities involved, the Hamiltonian of the Kovalevskaya top has no free parameter; hence mathematically there is only a single case to be considered. In phase space $T^*SO(3)$, the Hamiltonian reads

$$\mathcal{H}(\phi, \boldsymbol{\pi}) = \frac{(\pi_\varphi - \pi_\psi \cos \vartheta)^2}{4 \sin^2 \vartheta} + \frac{\pi_\vartheta^2}{4} + \frac{\pi_\psi^2}{2} - \sin \psi \sin \vartheta, \quad (1)$$

whereas in the reduced phase space, it is

$$\mathcal{H}(\boldsymbol{\gamma}, \boldsymbol{l}) = \frac{l_1^2}{4} + \frac{l_2^2}{4} + \frac{l_3^2}{2} - \gamma_1. \quad (2)$$

Note that the stable equilibrium position $\gamma_1 = 1$ is obtained for Euler coordinates $(\vartheta, \psi) = (\pi/2, \pi/2)$, with arbitrary φ . This means that the body-fixed axis e_1 points downward in the gravitational field, in agreement with the assumption made about the position of the center of mass. The unstable equilibrium $\gamma_1 = -1$ is given by $(\vartheta, \psi) = (\pi/2, 3\pi/2)$. While in the reduced phase space T^*S^2 both equilibria are single *points*, there exist whole φ -circles of equilibrium points in $T^*SO(3)$.

To obtain a physical realization of the Kovalevskaya top, we may proceed as follows, see Figure 1.

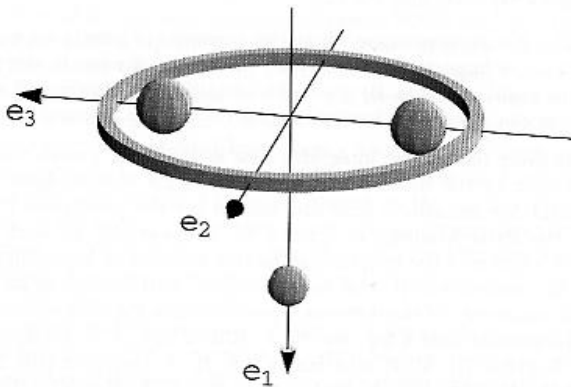


Fig. 1 Physical model of a Kovalevskaya top.

Take a ring of mass $2m$ and radius r , and let its symmetry axis be e_1 . Its center is chosen as fixed point and origin of the two frames of reference K and K' . The axes e_2 and e_3 lie in the plane of the ring. The moments of inertia of the ring are $(\theta_1, \theta_2, \theta_3) = (2, 1, 1)mr^2$. Now fix two weights on the 3-axis, such that each one has moment of inertia mr^2 with respect to the axes e_1 and e_2 , and a third weight on the 1-axis, again with moment of inertia mr^2 with respect to the axes e_2 and e_3 . Adding up, we find that the total arrangement has moments of inertia

$$(\Theta_1, \Theta_2, \Theta_3) = (4, 4, 2)mr^2, \quad (3)$$

and the center of mass is on the 1-axis, $\mathbf{c} = -c\mathbf{e}_1$ (the negative sign comes in by definition). If M is the total mass, then Mgc is a convenient unit for energies, and $\sqrt{\Theta_3/Mgc}$ a convenient unit for time. Angular momenta are then measured in units of $\sqrt{\Theta_3 Mgc}$, and moments of inertia in units of Θ_3 . With this choice of scales, the model is described by the Hamiltonians (1) or (2).

At low energies, $0 \leq h+1 \ll 1$, the motion may be discussed in terms of an expansion of the Hamiltonian around the stable equilibrium position, $(\vartheta, \psi) = (\pi/2, \pi/2)$. To second order in the phase space variables, using $\delta\vartheta := \vartheta - \pi/2$ and $\delta\psi := \psi - \pi/2$, we find

$$\mathcal{H} + 1 \approx \frac{1}{4}\pi_\varphi^2 + \frac{1}{4}\pi_\vartheta^2 + \frac{1}{2}(\delta\vartheta)^2 + \frac{1}{2}\pi_\psi^2 + \frac{1}{2}(\delta\psi)^2 = \mathcal{H}_\varphi + \mathcal{H}_\vartheta + \mathcal{H}_\psi. \quad (4)$$

This separates in the three coordinates $(\varphi, \vartheta, \psi)$. If all available energy $h+1$ is spent in only one of the three degrees of freedom, the system performs the corresponding pure type of motion:

1. φ -rotation about the vertical axis, with frequency $\omega_\varphi = \sqrt{h+1}$.
2. ϑ -oscillation about the axis \mathbf{e}_2 which does not move but may point in any horizontal direction. The frequency of these oscillations is $\omega_\vartheta = 1/\sqrt{2}$.
3. ψ -oscillation about the axis \mathbf{e}_3 . Again there is degeneracy with respect to all horizontal directions. The frequency is $\omega_\psi = 1$.

In action representation, this low energy limit of the Hamiltonian reads

$$\mathcal{H}(I_\varphi, I_\vartheta, I_\psi) = \frac{1}{4}I_\varphi^2 + \frac{1}{\sqrt{2}}I_\vartheta + I_\psi. \quad (5)$$

If the energy $h+1$ is shared among the three modes of motion, we observe linear superpositions. However, as h increases, the system is no longer separable in configuration space, and although it remains integrable, the motion becomes very complex.

At high energies, we may neglect the potential energy; all spatial directions become equivalent. The system approaches the behavior of a symmetric Euler top. As is well known, the non-symmetric Euler top performs stable rotations about the two principal axes with minimum and maximum moments of inertia; rotations about the axis with the intermediate Θ are unstable. In the film, we observe stable rotations about the 3-axis, but when initial conditions are chosen such that the body rotates about the 1-axis, we find that the residual influence of gravitation causes precessional motion, and that the stability of this motion depends on the height of the center of mass in the gravitational field; it is unstable if the center is too high.

These are but the first indications of complex behavior. In order to get a comprehensive understanding, the system will be subject to detailed investigation. In Section 2, we begin with a discussion of the equations of motion. For almost all calculations it will be preferable to work in the reduced phase space, i.e., we shall treat the Kovalevskaya top as a two-degrees-of-freedom system, with l as a parameter. Our aim is to obtain a survey on all possible types of energy surfaces \mathcal{E}_{hl} , including the different ways in which they are

foliated by invariant tori T^2 . This task is broken down in two parts. In the first part, Section 3, we analyze the topology of \mathcal{E}_{hl} and show that depending on (h, l) , there exist four different non-trivial types. In the second part, Section 4, we study the nature and organization of tori within a given \mathcal{E}_{hl} . Their complicated scheme of bifurcations gives rise to altogether ten different types of foliation. To represent the tori pictorially, two approaches are used. First, single tori are considered in projection to configuration or angular momentum space. This gives a fair impression of their bewildering complexity but is no good starting point for a survey on all possible tori. The second approach, developed in Section 5, involves the use of Poincaré sections Σ_{hl} or \mathcal{P}_{hl} across all tori of a given energy surface. With this technique, the foliation of surfaces \mathcal{E}_{hl} may be grasped in a single picture. In a last step, and the last part of the film, we attempt to generate a pictorial impression of the complete energy surfaces \mathcal{E}_h in terms of animation series where all surfaces \mathcal{E}_{hl} for given h are shown, with angular momenta l varying continuously from 0 to their maximum possible values.

2 Basic Equations in Reduced Phase Space

The Hamiltonian $\mathcal{H}(\boldsymbol{x}) = \mathcal{H}(\boldsymbol{\phi}, \boldsymbol{\pi})$ of a heavy rigid body with a fixed point may be found in any textbook on classical mechanics. Let us recall the main steps in its derivation. First, the kinetic energy of rotation is expressed in terms of the body's angular velocity $\boldsymbol{\omega} = (\omega_1, \omega_2, \omega_3) \equiv (p, q, r)$, as¹

$$T = \frac{1}{2}\Theta_1 p^2 + \frac{1}{2}\Theta_2 q^2 + \frac{1}{2}\Theta_3 r^2. \quad (6)$$

Second, the connection between $\boldsymbol{\omega}$ and Euler angles is derived from the kinematics of orthogonal transformations,

$$\boldsymbol{\omega} = \begin{pmatrix} p \\ q \\ r \end{pmatrix} = \begin{pmatrix} \sin \psi \sin \vartheta & \cos \psi & 0 \\ \cos \psi \sin \vartheta & -\sin \psi & 0 \\ \cos \vartheta & 0 & 1 \end{pmatrix} \begin{pmatrix} \dot{\phi} \\ \dot{\vartheta} \\ \dot{\psi} \end{pmatrix} =: \boldsymbol{\Phi} \dot{\boldsymbol{\phi}}. \quad (7)$$

Third, one identifies the canonical momenta through

$$\boldsymbol{\pi} = \frac{\partial T}{\partial \dot{\boldsymbol{\phi}}} = \boldsymbol{\Phi}^t \boldsymbol{\Theta} \boldsymbol{\Phi} \dot{\boldsymbol{\phi}}. \quad (8)$$

Expressing T as a function of $\boldsymbol{\phi}$ and $\boldsymbol{\pi}$, the kinetic part of Equ. (1) is obtained, if $\Theta_1 = \Theta_2 = 2\Theta_3$ is used together with proper scaling. To obtain the potential energy, use $V = Mg\boldsymbol{\gamma} \cdot \mathbf{c} = -Mg c \gamma_1$ and $\gamma_1 = \sin \psi \sin \vartheta$. The equations of motion are then derived with the standard symplectic structure matrix \mathbf{J} ,

$$\begin{pmatrix} \dot{\boldsymbol{\phi}} \\ \dot{\boldsymbol{\pi}} \end{pmatrix} = \begin{pmatrix} \mathbf{0} & \mathbf{1} \\ -\mathbf{1} & \mathbf{0} \end{pmatrix} \begin{pmatrix} \partial \mathcal{H} / \partial \boldsymbol{\phi} \\ \partial \mathcal{H} / \partial \boldsymbol{\pi} \end{pmatrix}, \quad \text{or} \quad \dot{\boldsymbol{x}} = \mathbf{J} \frac{\partial \mathcal{H}}{\partial \boldsymbol{x}}. \quad (9)$$

¹We stick to the classical notation (p, q, r) even though nowadays one might prefer the notation $(\omega_1, \omega_2, \omega_3)$.

This will not be done explicitly in the following, as the reduced description is much more convenient.

However, the components $(\boldsymbol{\gamma}, \mathbf{l})$ of the reduced phase space P_l are *not* canonically conjugated. Hence the energy function (2) is not a Hamiltonian in the canonical sense. But if the standard symplectic structure matrix \mathbf{J} is replaced by a suitable Poisson structure matrix \mathbf{J}_p , the simple function (2) can again be considered a Hamiltonian. To derive the appropriate matrix \mathbf{J}_p , consider the transformation $(\boldsymbol{\phi}, \boldsymbol{\pi}) \mapsto (\boldsymbol{\gamma}, \mathbf{l})$ given by the identities

$$\begin{pmatrix} \gamma_1 \\ \gamma_2 \\ \gamma_3 \end{pmatrix} = \begin{pmatrix} \sin \psi \sin \vartheta \\ \cos \psi \sin \vartheta \\ \cos \vartheta \end{pmatrix} \quad \text{and} \quad \begin{pmatrix} l_1 \\ l_2 \\ l_3 \end{pmatrix} = \begin{pmatrix} \Theta_1 p \\ \Theta_2 q \\ \Theta_3 r \end{pmatrix} = \Phi^{-1t} \dot{\boldsymbol{\pi}}. \quad (10)$$

Let \mathbf{M} be the Jacobian matrix of this transformation,

$$\mathbf{M} = \frac{\partial(\boldsymbol{\gamma}, \mathbf{l})}{\partial(\boldsymbol{\phi}, \boldsymbol{\pi})}; \quad (11)$$

it is then straightforward to see that

$$\mathbf{J}_p = \mathbf{M} \mathbf{J} \mathbf{M}^t = \begin{pmatrix} \mathbf{0} & \boldsymbol{\Gamma} \\ -\boldsymbol{\Gamma}^t & \boldsymbol{\Lambda} \end{pmatrix} \quad (12)$$

where $\boldsymbol{\Gamma}$ and $\boldsymbol{\Lambda}$ are antisymmetric matrix representations of $\boldsymbol{\gamma}$ and \mathbf{l} , respectively,

$$\boldsymbol{\Gamma} = \begin{pmatrix} 0 & -\gamma_3 & \gamma_2 \\ \gamma_3 & 0 & -\gamma_1 \\ -\gamma_2 & \gamma_1 & 0 \end{pmatrix} \quad \text{and} \quad \boldsymbol{\Lambda} = \begin{pmatrix} 0 & -l_3 & l_2 \\ l_3 & 0 & -l_1 \\ -l_2 & l_1 & 0 \end{pmatrix}. \quad (13)$$

The equations of motion are then obtained from the Hamiltonian (2) with

$$\begin{pmatrix} \dot{\boldsymbol{\gamma}} \\ \dot{\mathbf{l}} \end{pmatrix} = \begin{pmatrix} \mathbf{0} & \boldsymbol{\Gamma} \\ \boldsymbol{\Gamma} & \boldsymbol{\Lambda} \end{pmatrix} \begin{pmatrix} \partial \mathcal{H} / \partial \boldsymbol{\gamma} \\ \partial \mathcal{H} / \partial \mathbf{l} \end{pmatrix}, \quad \text{or} \quad \dot{\mathbf{y}} = \mathbf{J}_p \frac{\partial \mathcal{H}}{\partial \mathbf{y}}. \quad (14)$$

These equations are known as Euler-Poisson equations. The structure matrix \mathbf{J}_p has two Casimir functions $C_\gamma = \boldsymbol{\gamma} \cdot \boldsymbol{\gamma}$ and $C_l = \boldsymbol{\gamma} \cdot \mathbf{l}$. These functions are constants of *any* motion, by construction of the equations (14): For any phase space function $F(\mathbf{y})$, Equ. (14) implies

$$\dot{F} = \frac{\partial F}{\partial \mathbf{y}} \cdot \mathbf{J}_p \frac{\partial \mathcal{H}}{\partial \mathbf{y}} =: \{F, \mathcal{H}\}_p, \quad (15)$$

and for the Casimir functions we have

$$\mathbf{J}_p \frac{\partial C_\gamma}{\partial \mathbf{y}} = \mathbf{J}_p \frac{\partial C_l}{\partial \mathbf{y}} = 0. \quad (16)$$

Hence $\{C_\gamma, \mathcal{H}\}_p = \{C_l, \mathcal{H}\}_p$ for arbitrary Hamiltonians \mathcal{H} . The first Casimir constant reduces the three-dimensional $\boldsymbol{\gamma}$ -space to a two-dimensional $\boldsymbol{\gamma}$ -sphere, and for each $\boldsymbol{\gamma}$ the second Casimir constant defines the cotangent plane $\boldsymbol{\gamma} \cdot \mathbf{l} = \text{const}$ in \mathbf{l} -space. Any motion

is therefore restricted to a four-dimensional submanifold of P_l . The standard choice for the values of the Casimir functions is $C_\gamma = 1$ and $C_l = l$.

It is customary to write the Euler-Poisson equations in terms of angular velocity variables (p, q, r) . For the Kovalevskaya case this gives the two sets of equations

$$\begin{pmatrix} \dot{\gamma}_1 \\ \dot{\gamma}_2 \\ \dot{\gamma}_3 \end{pmatrix} = \begin{pmatrix} r\gamma_2 - q\gamma_3 \\ p\gamma_3 - r\gamma_1 \\ q\gamma_1 - p\gamma_2 \end{pmatrix} \quad \text{and} \quad \begin{pmatrix} 2\dot{p} \\ 2\dot{q} \\ \dot{r} \end{pmatrix} = \begin{pmatrix} qr \\ -rp - \gamma_3 \\ \gamma_2 \end{pmatrix}. \quad (17)$$

The transformation $(\phi, \pi) \mapsto (\gamma, l)$ in Equ. (10) is not invertible. From γ we may recover ϑ and ψ , and from l the canonical momenta $\pi = \Phi^t l$. But all information about φ has been discarded; the rank of the Jacobian matrix \mathbf{M} is 5. To find φ we must add to (17) its equation of motion from Equ. (9),

$$\dot{\varphi} = \frac{\partial \mathcal{H}}{\partial \pi_\varphi} = \frac{\pi_\varphi - \pi_\psi \cos \vartheta}{2 \sin^2 \vartheta} = \frac{l - l_3 \gamma_3}{2(\gamma_1^2 + \gamma_2^2)} = \frac{\gamma_1 p + \gamma_2 q}{\gamma_1^2 + \gamma_2^2}. \quad (18)$$

Once the time course of (γ, ω) has been determined, $\varphi(t)$ is obtained by quadrature (of hyperelliptic integrals!).

Equations (17) have four constants of motion. Two of them are the Casimir constants

$$\begin{aligned} C_\gamma &= \gamma_1^2 + \gamma_2^2 + \gamma_3^2 = 1, \\ C_l &= 2p\gamma_1 + 2q\gamma_2 + r\gamma_3 = l, \end{aligned} \quad (19)$$

the other two are the Hamiltonian \mathcal{H} and the Kovalevskaya constant K ,

$$\begin{aligned} \mathcal{H} &= p^2 + q^2 + \frac{1}{2}r^2 - \gamma_1 = h \\ K &= (p^2 - q^2 + \gamma_1)^2 + (2pq + \gamma_2)^2 = k^2. \end{aligned} \quad (20)$$

The easiest way to check their constancy is to compute the Poisson bracket $\{F, \mathcal{H}\}_p$ of any of these functions F with \mathcal{H} . The existence of these four conserved quantities, via the Liouville-Arnold theorem [2], implies that for generic values of (h, l, k^2) the motion in reduced phase space is restricted to one (or several) invariant 2-tori \mathcal{T}_{hlk} . Note that h can assume any value $h \geq -1$, and that by Equ.(20) we have $k^2 \geq 0$.

The equations of motion (17) are *not* invariant under time reversal T ,

$$T : (\gamma_1, \gamma_2, \gamma_3, p, q, r, t) \mapsto (\gamma_1, \gamma_2, \gamma_3, -p, -q, -r, -t), \quad (21)$$

except for $l = 0$. The operation T leaves C_γ , \mathcal{H} , and K constant but changes the sign of C_l . This behavior allows us to obtain results for $l < 0$ from those at $l > 0$. Therefore we shall restrict the discussion to $l \geq 0$.

There are two discrete symmetries that involve time reversal together with certain spatial reflections. One is

$$S_2 : (\gamma_1, \gamma_2, \gamma_3, p, q, r, t) \mapsto (\gamma_1, -\gamma_2, \gamma_3, p, -q, r, -t). \quad (22)$$

It is easy to see that this transformation leaves (h, l, k^2) invariant. Less obvious is the fact that each individual invariant torus respects this symmetry as well. The operation

$$S_3 : (\gamma_1, \gamma_2, \gamma_3, p, q, r, t) \mapsto (\gamma_1, \gamma_2, -\gamma_3, p, q, -r, -t) \quad (23)$$

is also a symmetry in the sense that (h, l, k^2) are left invariant. But it turns out that individual tori may break this symmetry. If so, they occur in pairs $\mathcal{T}_{hlk}^1, \mathcal{T}_{hlk}^2$ such that $\mathcal{T}_{hlk}^2 = S_3 \mathcal{T}_{hlk}^1$.

When the motion of φ is added via Equ. (18), the invariant 2-tori in T^*S^2 become 3-tori in $T^*SO(3)$. Thus a general orbit has two frequencies if considered in reduced phase space, and three in the full phase space. Several degrees of criticality are possible where tori become degenerate and change their topological character:

1. A torus $\mathcal{T}_{hlk} \subset T^*S^2$ turns into a circle. The motion is periodic in the reduced phase space and generically quasi-periodic, with only two frequencies, in $T^*SO(3)$.
2. A torus $\mathcal{T}_{hlk} \subset T^*S^2$ degenerates to a point. This is called a *relative equilibrium*. In the reduced phase space there is no motion at all, the full motion is nothing but a rotation in φ .
3. The motion may come to a complete stop. This happens at *absolute equilibria* of which there are only two cases, stable equilibrium at $(h, l, k^2) = (-1, 0, 1)$, and unstable equilibrium at $(h, l, k^2) = (1, 0, 1)$.

3 The four types of energy surfaces

3.1 Relative Equilibria

As stated above, relative equilibria are defined as fixed point solutions of Equ. (17), i.e., $\dot{\gamma} = \dot{l} = 0$. They exist only for special combinations of (h, l) which shall now be determined as lines in a (h, l^2) bifurcation diagram. It will be shown that the energy surfaces \mathcal{E}_{hl} change their topological character across these lines.

From $\dot{r} = \gamma_2 = 0$ all relative equilibria must have $\gamma_2 = 0$, and from $\dot{p} = 0$ we infer $qr = 0$. Let us distinguish the cases $r = 0$ and $q = 0$.

With $r = 0$ we conclude $\gamma_3 = 0$ (from $\dot{q} = 0$) and $q = 0$ (from $\dot{\gamma}_3 = 0$). Altogether,

$$\gamma_2 = \gamma_3 = q = r = 0. \quad (24)$$

From the two Casimir functions we get $\gamma_1^2 = 1$ and $2p\gamma_1 = l$. This specifies two possible types of motion:

H: $\gamma_1 = 1$: The potential energy assumes its minimum value -1 , the top rotates around its axis e_1 as a “sleeping top in hanging position”. Considering l as a free parameter, we have

$$p = l/2, \quad h = -1 + l^2/4, \quad k^2 = (h + 2)^2. \quad (25)$$

U: $\gamma_1 = -1$: The potential energy assumes its maximum value +1, the top rotates around its axis e_1 as a “sleeping top in upright position”,

$$p = -l/2, \quad h = 1 + l^2/4, \quad k^2 = (h - 2)^2. \quad (26)$$

It will be seen that the sleeping motion in hanging position is stable whereas in the upright position it is always unstable. The type of instability in the latter case is different for $l^2 < 4$ and $l^2 > 4$. The transition between these two types of behavior is marked by the existence of a third line of relative equilibria where $r \neq 0$, cf. Figure 2.

This line is obtained with $q = 0$ and, using $\dot{q} = 0$ and $\dot{\gamma}_2 = 0$,

$$rp + \gamma_3 = 0, \quad p^2 + \gamma_1 = 0. \quad (27)$$

From the second equation we infer immediately $k^2 = 0$: in these relative equilibria the Kovalevskaya constant assumes its minimum possible value. Moreover, it is obvious that $\gamma_1 \leq 0$ which means the top is at least half upright. The center of mass is lifted above the fixed point and rotates along a circle of constant height around the z axis. As there is no further rotation, the motion is reminiscent of a merry-go-round. With $\gamma_3^2 = 1 - \gamma_1^2$ we obtain $r^2 p^2 = 1 - p^2$ which leads to the following parametrization of the third bifurcation line:

$$\text{M: } l = -p^3 - \frac{1}{p}, \quad h = \frac{3}{2}p^2 + \frac{1}{2p^2}, \quad k^2 = 0. \quad (28)$$

The value of p varies in the range $0 \leq p^2 \leq 1$; the sign of p determines the sign of l . For $p \rightarrow 0$, the line goes to infinity along the direction $h \approx l^2/2 + 1/2l^2$. As p grows towards $p_c = \sqrt[4]{1/3} = 0.7598$, it reaches a cusp determined from $\partial h / \partial p = 0 = \partial l / \partial p$. The location of the cusp is

$$(h_c, l_c^2) = (\sqrt{3}, 16\sqrt{3}/9) = (1.7320, 3.0792). \quad (29)$$

At slightly lower p , namely for $p^2 = p_i^2 = \sqrt{2} - 1$, the line intersects the bifurcation line (26) in the point

$$(h_i, l_i^2) = (2\sqrt{2} - 1, 8(\sqrt{2} - 1)) = (1.8284, 3.3137). \quad (30)$$

(But note that in the full space of constants (h, l, k^2) , there is no intersection because the values of k^2 are different along the two lines.) For $p_c < p < 1$, we obtain a short line segment between (h_c, l_c^2) and the point

$$(h_m, l_m^2) = (2, 4) \quad (31)$$

where the third bifurcation line merges with the upright sleeping top.

The value of γ_1 for the merry-go-round motion is

$$\gamma_1^* = -\frac{h}{3} \pm \frac{1}{3}\sqrt{h^2 - 3}. \quad (32)$$

The + sign applies to the long branch where γ_1^* varies from 0 at infinity (center of mass at the same height with the fixed point) to $-1/\sqrt{3}$ at the cusp. Here the axis e_1 forms an angle of 54.7° with the vertical. On the small segment, the - sign applies, and as $h \rightarrow 2$, γ_1^* approaches the value -1 corresponding to upright position of the center of mass. With γ_1^* we know the frequency of the φ -rotation,

$$\dot{\varphi} = \frac{l}{1 + \gamma_1^{*2}}. \quad (33)$$

We shall see that the merry-go-round motion M is *stable* along the long branch (which will be called sM), and *unstable* along the short branch (uM) of the bifurcation line.

3.2 Bifurcations of energy surfaces

It is important to realize that the three bifurcation lines so determined divide the (h, l^2) plane into five regions with topologically different energy surfaces \mathcal{E}_{hl} . One of them is trivial: for $h < -1 + l^2/4$ the energy surface is the empty set, i.e., to the left of the line (25), no real motion exists (the rotational energy would exceed the total available energy). The other four topological types are given in Figure 2.

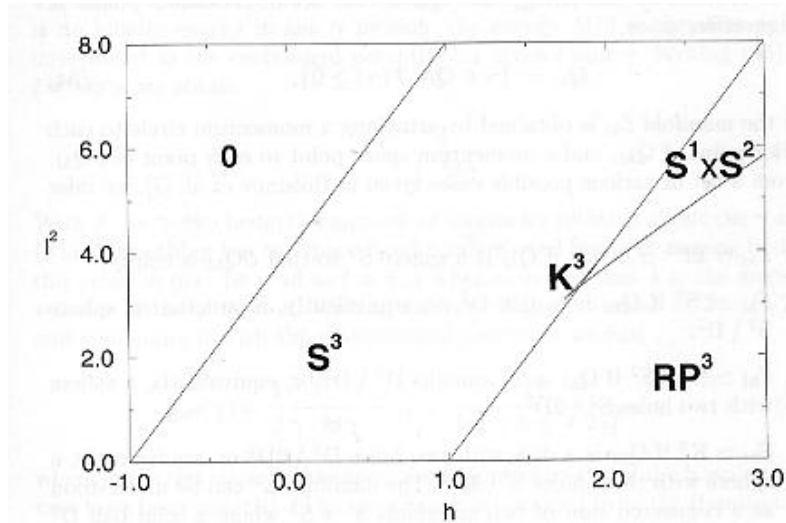


Fig. 2 (h, l^2) bifurcation diagram of energy surfaces \mathcal{E}_{hl} . – In the film, the size of region K^3 is exaggerated for better visibility.

They are a 3-sphere S^3 in the low- h , high- l region; a projective space $\mathbb{RP}^3 \simeq SO(3)$ in the high- h , low- l region; a direct product $S^1 \times S^2$ in the high- h , intermediate- l region, and a somewhat complicated manifold K^3 in the tiny region between the cusp of the third bifurcation line and its common points with the second. How can we determine the topology of the various \mathcal{E}_{hl} ?

According to Smale [29], the manifold structure of an energy surface is most readily understood as a bundle (with singular fibers) over the accessible part of configuration space. Considering the reduced configuration space after separation of the φ motion, we have a system with two degrees of freedom and variables $\boldsymbol{\gamma} \in Q_l \simeq S^2$. For given l , there exists an effective potential function $V_{\text{eff}}(\boldsymbol{\gamma})$ on this sphere which combines the influences of gravity and of fictitious inertial forces $\propto l^2$. Let the total energy be h , and consider a point $\boldsymbol{\gamma}$. If $h - V_{\text{eff}}(\boldsymbol{\gamma}) =: T(\boldsymbol{\gamma}) > 0$, then T is available as kinetic energy, and its value, together with the Casimir constant C_l , determines a circle in the space of momenta \mathbf{l} . If $T(\boldsymbol{\gamma}) = 0$, this circle shrinks to a point – the motion comes to a stop at this $\boldsymbol{\gamma}$ –, and if $T(\boldsymbol{\gamma}) < 0$, $\boldsymbol{\gamma}$ cannot be reached at this energy. Let Q_{hl} be the set of accessible points in configuration space,

$$Q_{hl} := \{\boldsymbol{\gamma} \in Q_l : T(\boldsymbol{\gamma}) \geq 0\}, \quad (34)$$

then the manifold \mathcal{E}_{hl} is obtained by attaching a momentum circle to each interior point of Q_{hl} , and a momentum space point to each point of ∂Q_{hl} .

From a list of various possible cases given in Bolsinov et al. [7], we infer that

1. $\mathcal{E}_{hl} \simeq \mathbb{RP}^3 \simeq \text{SO}(3)$ if Q_{hl} is a sphere S^2 so that ∂Q_{hl} is empty;
2. $\mathcal{E}_{hl} \simeq S^3$ if Q_{hl} is a disk D^2 or, equivalently, a punctuated sphere $S^2 \setminus D^2$;
3. $\mathcal{E}_{hl} \simeq S^1 \times S^2$ if Q_{hl} is an annulus $D^2 \setminus D^2$ or, equivalently, a sphere with two holes $S^2 \setminus 2D^2$;
4. $\mathcal{E}_{hl} \simeq K^3$ if Q_{hl} is a disk with two holes $D^2 \setminus 2D^2$ or, equivalently, a sphere with three holes $S^2 \setminus 3D^2$. The manifold K^3 can be understood as a connected sum of two manifolds $S^1 \times S^2$ where a solid ball D^3 has been removed from each copy and the two copies are then glued together along the boundary surfaces S^2 .

Let us now see how these four types of Q_{hl} , and thus the corresponding energy surfaces, occur in the Kovalevskaya system. The simplest case is $l = 0$ where the effective potential $V_{\text{eff}}(\boldsymbol{\gamma}) = -\gamma_1$ is nothing but the gravitational potential. Its level sets on the $\boldsymbol{\gamma}$ -sphere are the parallel circles $\gamma_1 = \text{const}$, with critical levels $h = -1$ and $h = 1$. The lower critical level is the stable *absolute* equilibrium; it marks the transition from an empty set to $Q_{hl} \simeq D^2$ and $\mathcal{E}_{hl} \simeq S^3$. The upper critical level is the unstable *absolute* equilibrium; it marks the transition from $Q_{hl} \simeq D^2 \simeq S^2 \setminus D^2$ to $Q_{hl} \simeq S^2$, and hence from energy surfaces S^3 to \mathbb{RP}^3 .

To determine the effective potential for $l \neq 0$ notice that the boundary ∂Q_{hl} for given (h, l) is characterized by the requirement that $\dot{\boldsymbol{\gamma}} = \boldsymbol{\gamma} \times \boldsymbol{\omega} = 0$, or that $\boldsymbol{\omega}$ be proportional to $\boldsymbol{\gamma}$,

$$\boldsymbol{\omega} = \Theta^{-1}\mathbf{l} = \lambda\boldsymbol{\gamma}, \quad (35)$$

where the real number λ is obtained by taking the scalar product with \mathbf{l} :

$$\lambda \mathbf{l} \cdot \boldsymbol{\gamma} = \lambda l = \mathbf{l} \cdot \Theta^{-1}\mathbf{l}. \quad (36)$$

The last expression is twice the kinetic energy. But when $\dot{\gamma} = 0$, there is no kinetic energy in the γ motion; the energy $\lambda l/2$ is therefore to be interpreted as the centrifugal potential for given l and γ . Writing (35) as $l = \lambda \Theta \gamma$, we obtain

$$\lambda = \frac{l}{\gamma \cdot \Theta \gamma}. \quad (37)$$

With $\theta_\gamma := \gamma \cdot \Theta \gamma$ being the moment of inertia for rotation about the γ axis (which is nothing but the space-fixed z -axis viewed from the moving body), this relation may be read as $l = \theta_\gamma \lambda$ whence we see that λ is the angular velocity of the φ motion. Writing the centrifugal potential $\lambda l/2 = l^2/2\theta_\gamma$ and combining it with the gravitational potential, we find

$$V_{\text{eff}}(\gamma) = \frac{1}{2} \frac{l^2}{\gamma \cdot \Theta \gamma} - \gamma_1 = \frac{l^2}{4\gamma_1^2 + 4\gamma_2^2 + 2\gamma_3^2} - \gamma_1, \quad (38)$$

where in the last equation the special moments of inertia of the Kovalevskaya case have been inserted. (The same result is obtained from the Hamiltonian (1) if the effect of $\pi_\varphi = l$ is separated into gyroscopic and centrifugal forces.) Eliminating γ_2 with $C_\gamma = 1$, we can express and draw the level lines as functions $\gamma_1 = \gamma_1(\gamma_3)$,

$$\gamma_1 = -V_{\text{eff}} + \frac{l^2/2}{2 - \gamma_3^2}. \quad (39)$$

On the circle $\gamma_3 = 0$ the effective potential decreases linearly with γ_1 , whereas on the circle $\gamma_2 = 0$ or $\gamma_3^2 = 1 - \gamma_1^2$ we have

$$V_{\text{eff}}(\gamma_2 = 0) = -\gamma_1 + \frac{l^2/2}{1 + \gamma_1^2}. \quad (40)$$

Depending on l^2 , this may or may not have relative extrema in the range $-1 < \gamma_1 < 0$, giving rise to critical points in the system of equipotential lines, and hence to topological changes of the accessible parts Q_{hl} on the γ -sphere. By elementary analysis, one determines four qualitatively different systems of contour lines, cf. the schematic drawings of level lines in the neighborhood of the north pole $\gamma_1 = -1$ in Figure 3.²

²There are thick and thin level lines on the γ -sphere in our film. The thick lines are chosen at equidistant levels of V_{eff} . The thin lines are taken at one tenth that level distance.

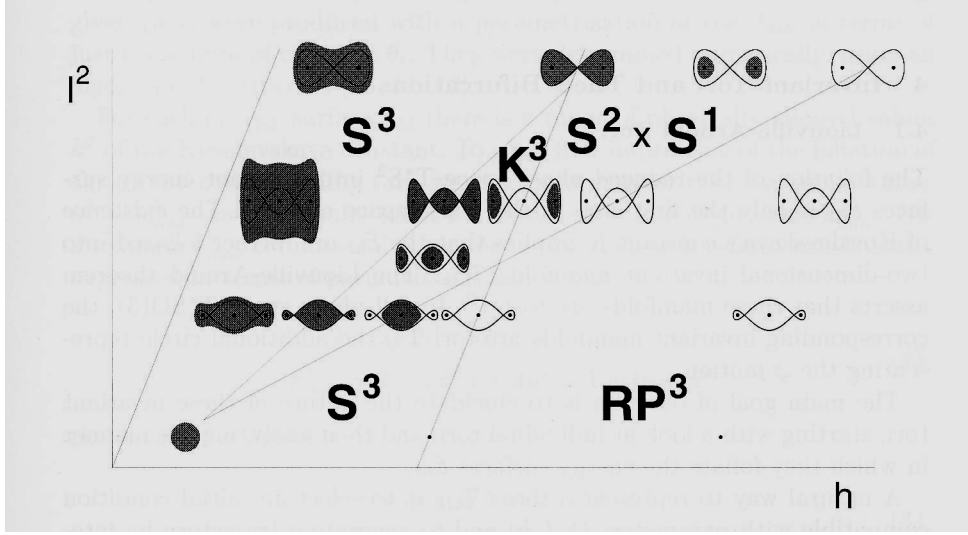


Fig. 3 The four types of level lines on the γ -sphere (schematic drawing). For representative values l^2 , the critical level lines of the effective potential are drawn as full lines. For given (h, l^2) , the shaded fields are the energetically *not* accessible regions. In each little diagram, the central dot is the north pole; the other dots are relative maxima. At low values of h , the entire neighborhood of the north pole is forbidden. As h increases, the holes in the γ -sphere become smaller and develop a pattern depending on l^2 . Eventually, in the (h, l^2) range marked \mathbb{RP}^3 , all γ are possible.

1. For $l^2 < l_c^2 = 3.0792$, the effective potential is everywhere decreasing with increasing γ_1 . Thus the two sleeping tops at $\gamma_1 = \pm 1$ with $h = -\gamma_1 + l^2/4$ are the only critical points on the γ -sphere. For $h < 1 + l^2/4$ the accessible part of Q_l is a disk, hence $\mathcal{E}_{hl} \simeq S^3$, for larger energies Q_{hl} is the whole sphere, hence $\mathcal{E}_{hl} \simeq \mathbb{RP}^3$.
2. For l in the small range $l_c^2 < l_i^2 = 3.3137$, $V_{\text{eff}}(\gamma_2 = 0)$ has two critical points γ_1^s, γ_1^m in the range $-1 < \gamma_1 < 0$. This implies that besides the absolute minimum at $\gamma_1 = 1$, there are two maxima at $\gamma = (\gamma_1^m, 0, \pm\sqrt{1 - (\gamma_1^m)^2})$, two saddles at $\gamma = (\gamma_1^s, 0, \pm\sqrt{1 - (\gamma_1^s)^2})$, and a maximum at $\gamma_1 = -1$. The maximum at $\gamma_1 = -1$ has *higher* effective potential than that at $\gamma_1 = \gamma_1^m$. Consequently, we find the following succession of Q_{hl} types, as h increases:

$$Q_{hl} : S^2 \setminus D^2 \simeq D^2 \rightarrow S^2 \setminus 3D^2 \rightarrow S^2 \setminus D^2 \rightarrow S^2.$$

The corresponding succession of energy surfaces is

$$\mathcal{E}_{hl} : S^3 \rightarrow K^3 \rightarrow S^3 \rightarrow \mathbb{RP}^3.$$

3. For $l_i^2 < l^2 < l_m^2 = 4$, the situation is similar except that the maximum at $\gamma_1 = -1$ has *lower* effective potential than that at $\gamma_1 = \gamma_1^m$. The succession of Q_{hl} types is

$$Q_{hl} : S^2 \setminus D^2 \simeq D^2 \rightarrow S^2 \setminus 3D^2 \rightarrow S^2 \setminus 2D^2 \rightarrow S^2;$$

the corresponding succession of energy surfaces is

$$\mathcal{E}_{hl} : S^3 \rightarrow K^3 \rightarrow S^1 \times S^2 \rightarrow \mathbb{RP}^3.$$

4. For $l^2 > 4$, $V_{\text{eff}}(\gamma_2 = 0)$ has a relative minimum at $\gamma_1 = 1$, and a maximum at $\gamma_1 = \gamma_1^m$ in the range $(-1, 0)$. This implies that the γ -sphere carries an absolute minimum at $\gamma_1 = 1$, a saddle at $\gamma_1 = -1$, and two maxima at $\gamma = (\gamma_1^m, 0, \pm\sqrt{1 - (\gamma_1^m)^2})$. The succession of Q_{hl} types is

$$Q_{hl} : S^2 \setminus D^2 \simeq D^2 \rightarrow S^2 \setminus 2D^2 \rightarrow S^2.$$

The corresponding succession of energy surfaces is

$$\mathcal{E}_{hl} : S^3 \rightarrow S^1 \times S^2 \rightarrow \mathbb{RP}^3.$$

The values of h where the Q_{hl} and hence the \mathcal{E}_{hl} change their topology are the critical values of $V_{\text{eff}}(\gamma_2 = 0)$ for given l . From the critical points $\gamma_1 = \pm 1$, we recover the bifurcation lines H and U of Section 3.1. The critical points γ_1^m and γ_1^s are the analytic extrema of the polynomial

$$P(\gamma_1) = 2(h + \gamma_1)(1 + \gamma_1^2) - l^2, \quad (41)$$

cf. Equ. (40). They bifurcate at points (h, l) where the discriminant Δ vanishes,

$$\Delta = \frac{27}{16}l^4 - \frac{1}{2}h(9 + h^2)l^2 + (1 + h^2)^2 = 0. \quad (42)$$

The same condition is obtained from Eqs. (28) if p is eliminated as a parameter. We see that relative equilibria and bifurcations of the energy surface give the same bifurcation lines. This is generically true.

4 Invariant tori and their bifurcations

4.1 Liouville-Arnold tori

The foliation of the reduced phase space T^*S^2 into invariant energy surfaces \mathcal{E}_{hl} is only the first step in the phase space analysis. The existence of Kovalevskaya's constant K implies that the \mathcal{E}_{hl} are further foliated into two-dimensional invariant manifolds \mathcal{T}_{hik} . The Liouville-Arnold theorem asserts that these manifolds are tori T^2 . In full phase space $T^*SO(3)$, the corresponding invariant manifolds are tori T^3 , the additional circle representing the φ motion.

The main goal of our film is to elucidate the nature of these invariant tori, starting with a look at individual tori, and then analyzing the manner in which they foliate the energy surfaces \mathcal{E}_{hl} .

A natural way to represent a torus \mathcal{T}_{hlk} is to select an initial condition compatible with parameters (h, l, k) and to generate a trajectory by integrating the equations of motion. Unless the winding number happens to be rational, this trajectory will eventually fill the torus densely. Various projections may be chosen for visualization. The film illustrates this with a trajectory for $(h, l^2, k^2) = (1.2, 1.58, 1.41)$ which is shown in projection onto the γ sphere, and into the space of angular momenta \mathbf{l} . The γ projection gives an idea of how the rigid body moves in real space, except that it ignores the φ motion. Because of its two-dimensional nature, it cannot give a fair impression of the toroidal nature of \mathcal{T}_{hlk} . This is possible in the \mathbf{l} projection, but even there, self-intersections along certain lines, and changes of orientation at these lines, cannot be avoided. To make these changes visible, the interior side of a torus is represented in dark, the outside in light colors.

Besides the mere existence of invariant tori \mathcal{T}_{hlk} , the Liouville-Arnold theorem provides a canonical set of corresponding coordinates, the *action angle variables* $(\theta_1, \theta_2, I_1, I_2)$. There exists a canonical transformation $(\phi, \pi) \mapsto (\theta, \mathbf{I})$ by which the Hamiltonian assumes the form $\mathcal{H} = \mathcal{H}(\mathbf{I})$. The associated equations of motion show that the I_i are constants of motion, and that the θ_i change at constant rates $\dot{\theta}_i = \partial\mathcal{H}/\partial I_i$. The I_i may be viewed as labelling the invariant tori while the closed loops $\theta_i = \text{const}$ are a natural set of coordinate lines on them. In practice, it is a difficult problem to determine these lines [11]; the film does not address these matters explicitly. However, the animated sequences with tori of varying k^2 at given (h, l) were produced with a parametrization of the \mathcal{T}_{hlk} in terms of just these lines of constant θ_i . They were determined numerically, using an algorithm described in [11, 9, 10].

For each energy surface \mathcal{E}_{hl} there is a range of physically allowed values k^2 of the Kovalevskaya constant. To get a first impression of the foliation of \mathcal{E}_{hl} by the corresponding tori, we start with the torus of maximum value, $k^2 = k_{\max}^2$, and gradually lower k^2 towards the minimum value k_{\min}^2 . The maximum k_{\max}^2 cannot easily be given in closed form; it is most conveniently expressed in terms of parameters h and $p \equiv \omega_1$,

$$\begin{aligned} l &= 2p(p^2 - h), \\ k_{\max}^2 &= 1 - 2p^2h + 3p^4 = 1 + lp + p^4; \end{aligned} \tag{43}$$

the range of p values is

$$\begin{aligned} 0 < p < \sqrt{h+1} &\quad \text{if } h < 0, \\ \sqrt{h} < p < \sqrt{h+1} &\quad \text{if } h > 0. \end{aligned} \tag{44}$$

The minimum values are

$$k_{\min}^2 = \begin{cases} (l^2/2 - h)^2 & \text{if } h < 0 \text{ or } l^2 > 2h, \\ 0 & \text{if } h > 0 \text{ and } l^2 < 2h. \end{cases} \tag{45}$$

For $k^2 = k_{\max}^2$ and $k^2 = k_{\min}^2$, the tori \mathcal{T}_{hlk} are *critical*, i.e., they degenerate to circles. The motion in reduced phase space is periodic, the full motion quasiperiodic, with a second period for the φ motion. In the \mathbf{l} projection, a critical torus is a closed line (which sometimes degenerates to a line segment because the projection superimposes two halves of the loop). In the simplest cases, $h < 0$, no further criticality occurs between k_{\max}^2 and k_{\min}^2 . Critical tori at (local) maximum and minimum values of k^2 are always *stable* isolated periodic orbits.

In a more typical case, another critical torus occurs at an intermediate value of k^2 , and there are various ways in which this may happen. In the first example of the film, $(h, l^2) = (1.2, 1.58)$, where $k_{\max}^2 = 5.468$ and $k_{\min}^2 = 0$, an *unstable* periodic orbit appears at a value $k^2 = k_{\text{sep}}^2 = 0.168$. It forms the center of a separatrix between different types of foliation. There is *one* torus \mathcal{T}_{hlk} for each value $k^2 > k_{\text{sep}}^2$, but *two* tori for each $k^2 < k_{\text{sep}}^2$. The tori bifurcate as k^2 is lowered through k_{sep}^2 . The two families of tori at $k^2 < k_{\text{sep}}^2$ are related by the symmetry S_3 , see (23); in the \mathbf{l} projection they are mirror images under $l_3 \rightarrow -l_3$. At the minimum value $k^2 = 0$ each family ends in a critical torus representing stable periodic motion in the reduced phase space.

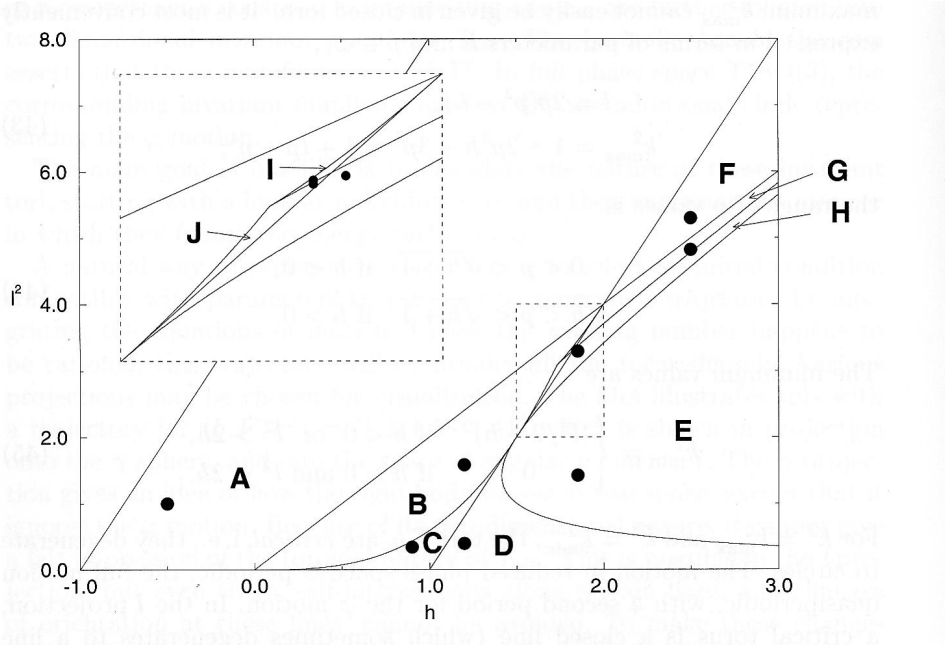


Fig. 4 Bifurcation diagram of energy surfaces and their foliations. The inset is a blowup of the rectangular region marked in the main figure. The dots refer to the choice of parameters (h, l^2) in the series of Poincaré sections shown in Figure 9. – The corresponding picture in the film is slightly deformed in order to better exhibit the fine structure in the blown-up region.

In general, as we vary the values (h, l) across the bifurcation diagram, the number and/or nature of critical tori changes at bifurcations of the energy surface \mathcal{E}_{hl} . Moreover,

tori may become critical within a given topological type of \mathcal{E}_{hl} . This gives rise to four further lines in the (h, l) bifurcation diagram, as shown in Figure 4. A detailed discussion of these lines is given in the following subsection. The figure shows that the set of all bifurcation lines defines 10 distinct regions in the (h, l) bifurcation diagram. We call them (h, l) -phases and introduce a scheme of letters A ... J to name these phases. Each one represents a particular type of foliation of \mathcal{E}_{hl} . The example $(h, l^2) = (1.2, 1.58)$ is taken from phase B.

4.2 Appelrot classes and Kharlamov regions

The set of *all* critical tori provides a kind of backbone around which the other tori are organized. Their identification and characterization has been a lifetime's work for G. G. Appelrot [1] who distinguished four classes I through IV, with many subtypes. Appelrot's analysis was based on the representation of Kovalevskaya's dynamics in terms of hyperelliptic functions [26]. A more straightforward method to obtain the bifurcation diagram was applied by M. P. Kharlamov [16] who studied critical values of the energy-momentum mapping $(\gamma, l) \mapsto (h, k, C_l, C_\gamma)$. Kharlamov introduced a scheme of numbers i through v to denote regions in (h, l, k) space, called (h, l, k) -phases, corresponding to different types of foliation of the reduced phase space T^*S^2 . The Appelrot tori form the boundaries of the Kharlamov regions.

A third method, based on the analysis of isolated periodic orbits in an appropriate Poincaré map, was introduced in [9, 10]. Its advantage is the explicit characterization of the various types of tori in each region of the bifurcation diagram.

A comprehensive and quantitative representation of all critical tori requires a three-dimensional (h, l, k) bifurcation diagram, but this is cannot easily be produced. Instead, we offer in Figures 5 and 6 two-dimensional slices at 8 typical values of energy h , corresponding to different types of energy surfaces \mathcal{E}_h . We call these slices (l, k) bifurcation diagrams.

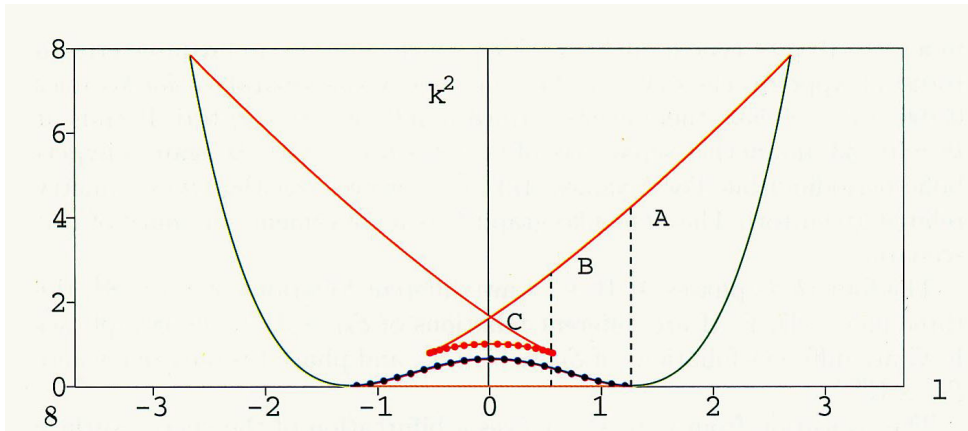


Fig. 5 (l, k^2) bifurcation diagram for $h = 0.8$.

Figure 5 is an example of such a slice, with $h = 0.8$, in the “natural” variables l and k^2 . The entire range of positive and negative values of l is shown to exhibit the symmetry under $l \rightarrow -l$, and the way in which the lines continue across $l = 0$. In the series of Figures 6, the $l < 0$ part is omitted, and instead of k^2 we plot k in order to have all individual pictures on the same scale. Note that this transformation turns the smooth minimum at the junction of green and blue lines, at $(l, k) = (\sqrt{2h}, 0)$, into an artificial cusp.

The figures exhibit lines in four colors, called *Appelrot lines*. They correspond to the four classes of critical orbits defined by Appelrot: I (orange), II (green), III (blue), and IV (red). Full lines are stable, lines carrying dots are unstable critical tori. Points where Appelrot lines intersect transversally, in the (l, k^2) representation to be precise, mark bifurcations of \mathcal{E}_{hl} , i. e., relative equilibria. Tangencies of Appelrot lines mark bifurcations of critical tori as discussed below on page 26. The corresponding values of l separate different (h, l) -phases A, ..., J, cf. Figure 4. Regions enclosed by the Appelrot lines are Kharlamov’s (h, l, k) -phases. In Figures 6, they are given the colors red (i), green (ii), yellow (iii), blue (iv), and purple (v). Some of these phases appear disconnected in a given (l, k) slice, yet in the full (h, l, k) space they form a single connected region.

The pictures of Figures 6b contain blow-ups (even two successive stages in the case of $h = 1.42$) in order to display the very intricate features in the parameter range $1 < l, h < 2$.

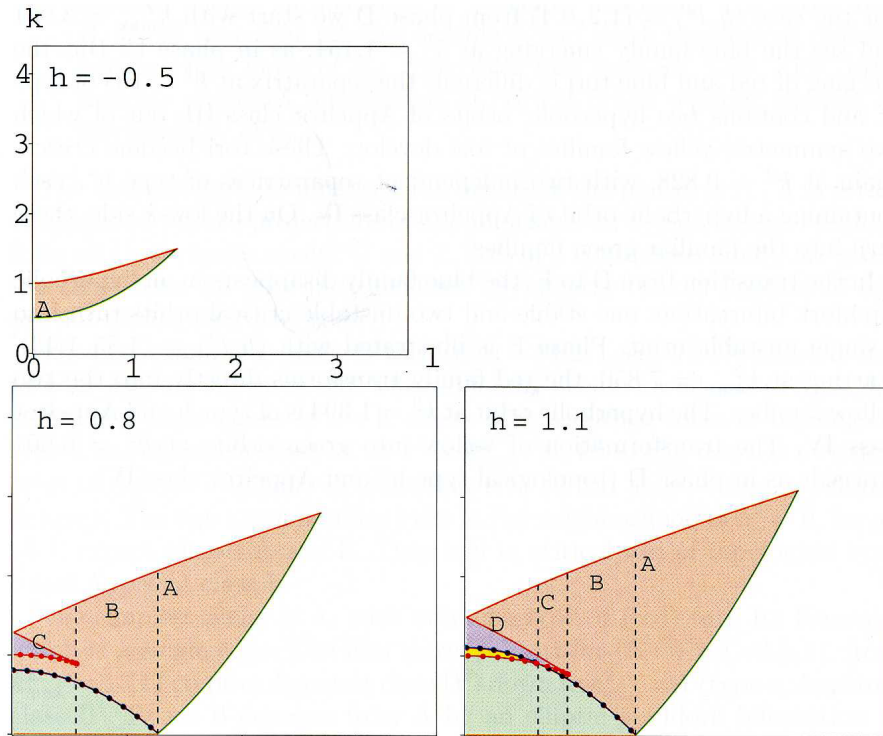


Fig. 6a: (l, k) bifurcation diagrams for $h = -0.5$, $h = 0.8$, and $h = 1.1$.

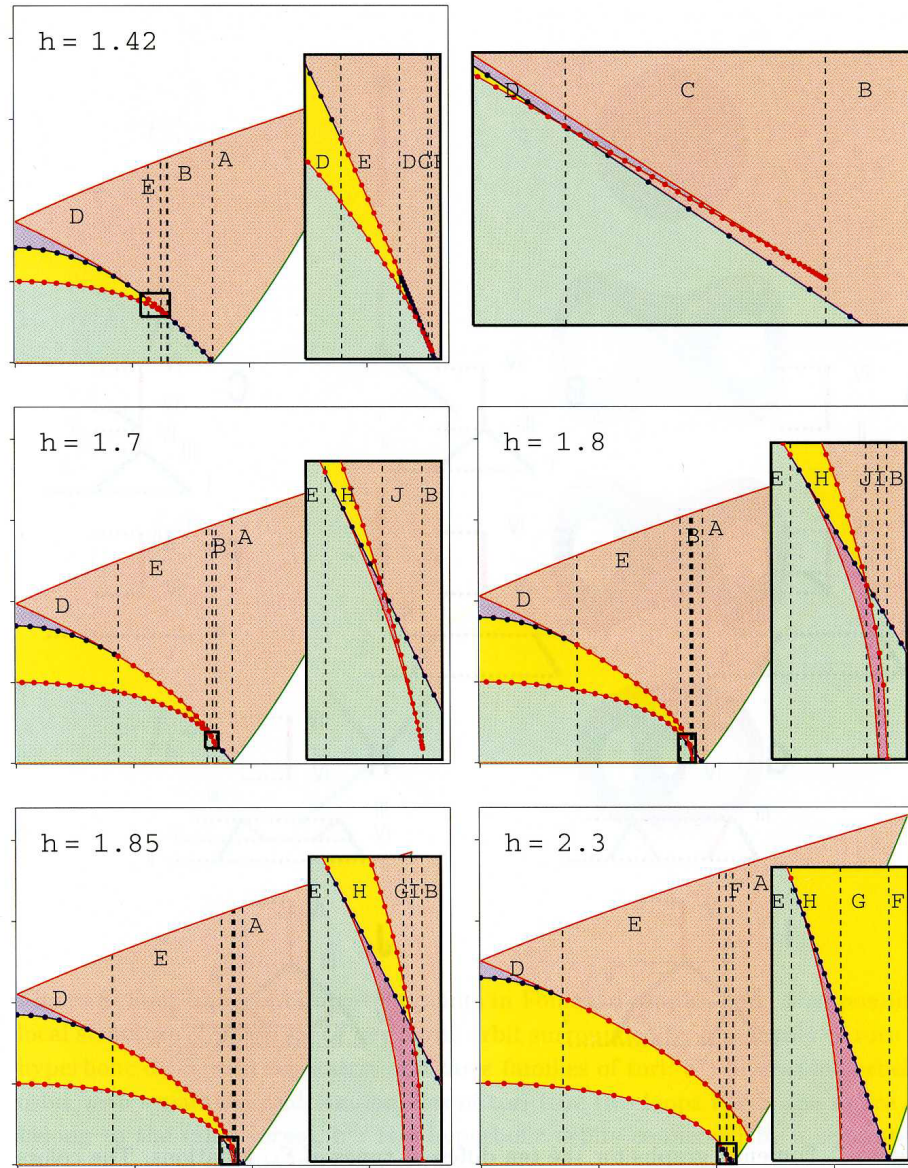


Fig. 6 b: (l, k) bifurcation diagrams for energies $h = 1.42, 1.7, 1.8, 1.85$, and 2.3 .

Explicit expressions for the Appelrot lines of classes I through IV have been derived in [9, 10], using the Poincaré surface of section discussed in Section 5. Here we only collect the results, including statements about the stability properties of the respective critical orbits in reduced phase space.

I: $k = 0$ in the l -range $0 < l < \sqrt{2h}$, $h > 0$. The corresponding critical tori are elliptic.

II: $k = l^2/2 - h$ in the l -range $\max(0, h) < l^2/2 < 2(h+1)$. Critical tori of class II have $k^2 = k_{\min}^2$ for given (h, l) , hence they are also elliptic.

III: $k = h - l^2/2$ in the l -range $0 < l^2/2 < h$, $h > 0$. For energies $h > \sqrt{2}$ and l -values in phase E,

$$h - \sqrt{h^2 - 2} =: l_-^2 \leq l^2 \leq l_+^2 := h + \sqrt{h^2 - 2}, \quad (46)$$

this Appelrot line does *not* correspond to critical tori. The special feature of these tori is that they are characterized by elliptic rather than hyperelliptic functions, but this is only of analytic, not of topological interest. These segments are therefore not shown in Figure 6. All critical tori of class III are hyperbolic.

IV: This is really a collection of different lines. Appelrot lumped them together because they are all parametrized by

$$\begin{aligned} l &= 2p(p^2 - h), \\ k^2 &= 1 - 2p^2h + 3p^4 = 1 + lp + p^4, \end{aligned} \quad (47)$$

cf. Equ. (43); they differ in the ranges of p . The piece where $k^2 = k_{\max}^2$, as defined in Equ. (44), is the only one with positive p ; in regions A and B there is no other Appelrot line of class IV. The other pieces, in phases C ... J, derive from p in the range $-\sqrt{h} < p < 0$ of negative values. The following is a description of the respective pieces in the eight different types of energy surfaces.

1. $h < 0$: stable critical tori (i.e., elliptic isolated periodic orbits) for $0 < p < \sqrt{h+1}$.
2. $0 < h < 1$: stable critical tori for $\sqrt{h} < p < \sqrt{h+1}$ (uppermost branch) and $-\sqrt{h} < p < -\sqrt{h/3}$ (second branch from above in phase C); unstable critical tori (i.e., hyperbolic isolated periodic orbits) for $-\sqrt{h/3} < p < 0$ (third branch). The cusp at $p = -\sqrt{h/3}$ marks a saddle-node bifurcation upon the transition between phases B and C. (The parameter range $0 < p < \sqrt{h}$ gives Appelrot line segments with negative l .)
3. $1 < h < \sqrt{2}$: the same as above, but here the third branch intersects the Appelrot line of class III at the transition from C to D (\mathcal{E}_{hl} changes its topology). In region D, the tori of the third branch are inverse hyperbolic orbits.
4. $\sqrt{2} < h < 1.5$: almost the same as in case 2, except that the second branch from above is hyperbolic in region E, i.e., for $-1/l_- < p < -1/l_+$. At the endpoints of this interval, the instability is transferred to critical tori of class III.

5. $1.5 < h < \sqrt{3}$: the second branch is stable for $-\sqrt{h} < p < -1/l_-$ (region D) and unstable for $-1/l_- < p < -\sqrt{h/3}$ (regions E, H, J); the third branch is stable for $-\sqrt{h/3} < p < -1/l_+$ (regions H and J), unstable for $-1/l_+ < p < 0$ (regions E and D).

Up to here, the cusp at $p = -\sqrt{h/3}$ has physical reality as a saddle-node bifurcation because it occurs for $k^2 > 0$. For larger values of h , the range $-p_2 < p < -p_1$ with $3p_{1,2}^2 = h \mp \sqrt{h^2 - 3}$ is spared out as it would lead to unphysical $k^2 < 0$. The two pieces $p < -p_2$ (upper branch) and $p > -p_1$ (lower branch) are disconnected.

6. $\sqrt{3} < h < 2\sqrt{2} - 1$: the second branch is stable for $-\sqrt{h} < p < -1/l_-$ (region D) and unstable for $-1/l_- < p < -p_2$ (regions E, H, J, I); the third branch is stable for $-p_1 < p < -1/l_+$ (regions H and J), unstable for $-1/l_+ < p < 0$ (regions E and D).
7. $2\sqrt{2} - 1 < h < 2$: same as in case 6 except that the order of the topological changes of \mathcal{E}_{hl} , as l grows, is changed. The second branch is stable for $-\sqrt{h} < p < -1/l_-$ (region D) and unstable for $-1/l_- < p < -p_2$ (regions E, H, G, I); the third branch is stable for $-p_1 < p < -1/l_+$ (region H), unstable for $-1/l_+ < p < 0$ (regions E and D).
8. $h > 2$: the second branch is stable for $-\sqrt{h} < p < -1/l_-$ (phase D) and unstable for $-1/l_- < p < -\sqrt{h-1}$ (phases E, H, G, F); the third branch is stable for $-p_1 < p < -1/l_+$ (region H), unstable for $-1/l_+ < p < 0$ (regions E and D).

An additional important piece of information is that the number of different tori for a given triple of values (h, l, k) depends on the Kharlamov region. It is *one* in region i (red), *two* in regions ii (green), iii (yellow), iv (blue), and *four* in the tiny region v (purple).

4.3 Fomenko graphs and their bifurcations

Given the information collected in the previous subsection, it is straightforward to derive the type of foliation of \mathcal{E}_{hl} for each given phase A ... J. A qualitative picture of these foliations may be given in terms of a classification scheme developed by A. T. Fomenko [13]. There an energy surface \mathcal{E}_{hl} is depicted as a graph in which each point represents a torus. We choose the height of a point in the graph to indicate the value of the Kovalevskaya constant. The tori of a continuous family form an edge of the graph. End points correspond to stable, branch points to unstable isolated periodic orbits. The Fomenko graph associated with $(h, l) = (1.2, 1.58)$ is characteristic of the (h, l) -phase B and has the form

of a letter Y turned upside down. Figure 7 collects the graphs for all 10 phases.

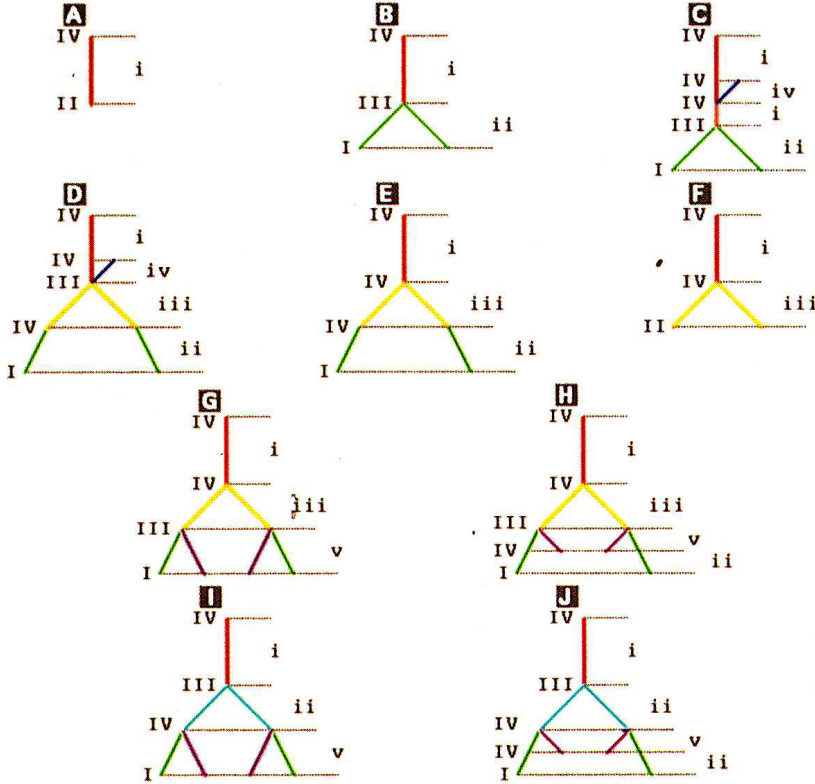


Fig. 7 Fomenko graphs for the ten different types of \mathcal{E}_{hl} foliations. The colors identify continuous families of tori. Also shown are numbers I through IV to denote the Appelrot classes of critical tori, and numbers i through v to denote Kharlamov's (h, l, k) -phases.

From our discussion of the stability properties of critical tori (especially of Appelrot class IV) it is clear that the Appelrot classification has no direct topological interpretation. On the other hand, the nature of a critical point in Fomenko's diagrams tells a great deal about the corresponding critical torus and its neighborhood in phase space. From the topological point of view, the Kovalevskaya system possesses (again) four different types of critical tori. Figure 8 collects them together with sketches of the organization of their phase space neighborhoods. The pictures must be interpreted as transverse intersections of the critical tori (and, in case of hyperbolic orbits, of the associated separatrices) in the energy surfaces \mathcal{E}_{hl} .

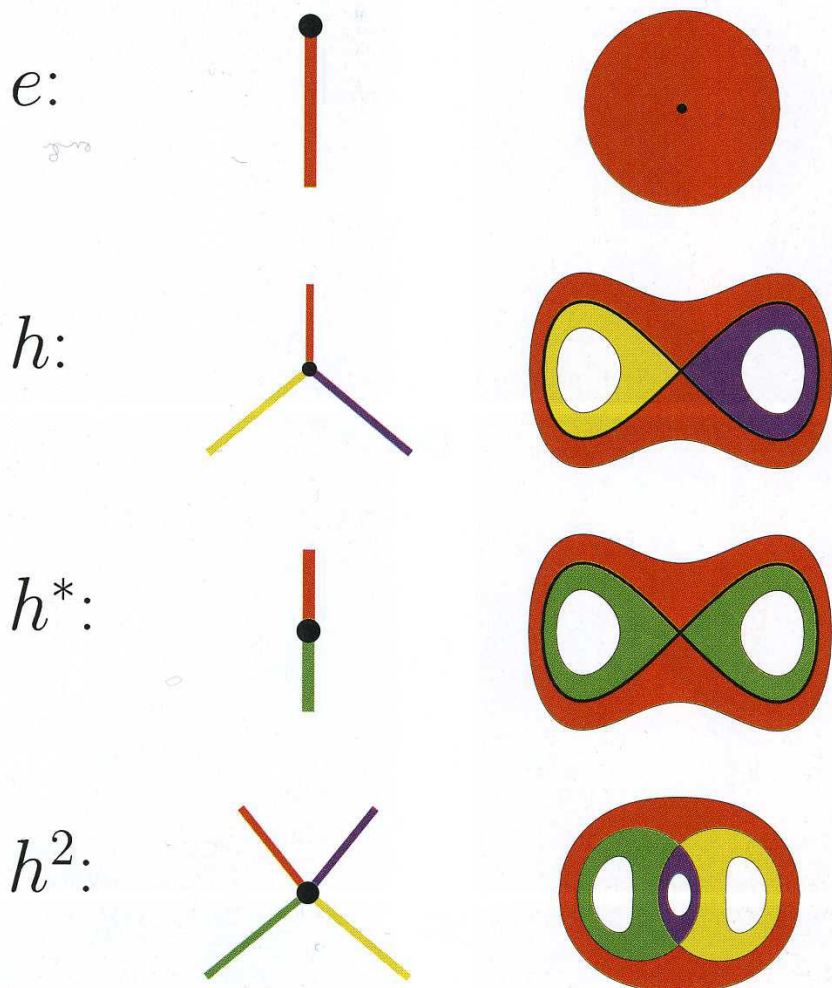


Fig. 8 Four types of bifurcation points in Fomenko graphs, and corresponding local structure of phase space. e: elliptic orbit surrounded by *one* family of tori; h: hyperbolic orbit with separatrix and *three* families of tori; h^* : inverse hyperbolic orbit with separatrix and *two* families of tori (the two loops inside the figure ∞ belong to the same torus); h^2 : two hyperbolic orbits connected by a separatrix and surrounded by *four* families of tori.

The four topological types of critical orbits are the following.

- e: Free end points of edges. They correspond to elliptic isolated periodic orbits and are surrounded by nested tori. (In Fomenko's nomenclature they are called *atoms* A.)
- h: Branch point where *three* edges meet. In phase space, this corresponds to an hyperbolic isolated periodic orbit with two homoclinic connections forming the separatrix between three families of tori. (Fomenko's *atom* B.)
- h^* : Critical point where *two* edges meet. The isolated critical orbit is inverse hyperbolic and has one homoclinic connection which separates two families of tori. (Fomenko's *atom* A*.)
- h^2 : Branch point with *four* emanating edges. In phase space there are two hyperbolic isolated periodic orbits, with four heteroclinic connections separating four families of tori. (Fomenko's *atom* C₂.)

The Appelrot classes I and II are always of topological type e. Class III is of type h in phases B, C, G, H, I, J, and of type h^2 in phase D; in phase E the class III tori are not even critical. Appelrot class IV comes in three different topological types: type e in all phases for $k^2 = k_{\max}^2$, and furthermore in phases C, D, H, J as centers of the blue and violet families of tori, respectively; type h in phases C, E, F, G, H, I, J; type h^* in phases D and E. This makes it obvious that Appelrot's analytical and Fomenko's topological viewpoints reveal different aspects of a system's dynamics.

While Figure 8 illustrates the various ways in which critical tori organize the bifurcation of *noncritical* tori, we shall now address the bifurcation behavior of *critical* tori, or, in other words, the changes of Fomenko graphs, or types of foliation, between neighboring phases. Such changes occur whenever Appelrot lines in Figure 6 intersect or have a tangency. It appears that transverse intersections indicate bifurcations of the energy surface \mathcal{E}_{hl} whereas bifurcations without topological changes of \mathcal{E}_{hl} involve tangencies of Appelrot lines.

When \mathcal{E}_{hl} changes its topology, at relative equilibria, the foliation may be affected in a variety of ways. Let us consider the cases identified in Section 3.1.

- H: The sleeping top in hanging position sits at the intersection of two elliptic Appelrot lines of classes II and IV. This corresponds to its being doubly elliptic in a linear stability analysis. The transition may be described as $2e \leftrightarrow \emptyset$.
- U: The sleeping top in upright position involves four different transitions, depending on the value of $h = 1 + l^2/4$. For $h > 2$, between phases A and F, the intersecting lines are elliptic and hyperbolic, respectively, corresponding to an elliptic-hyperbolic stability character. The transition is $e \leftrightarrow 2e + h$, as in an elliptic pitchfork bifurcation, see below. For $h < 2$, on the other hand, all intersecting lines are hyperbolic, corresponding to the doubly hyperbolic instability of U. In the range $1.5 < h < 2$

($I \leftrightarrow G$ and $J \leftrightarrow H$), the transition is $h + h \leftrightarrow h + h$, whereas for $1 < h < 1.5$ ($C \leftrightarrow D$) it is $h + h \leftrightarrow 2h^* + h^2$.

M: The merry-go-round motion occurs at the intersection of the elliptic line of Appelrot class I with stable or unstable segments of class IV. Between G and H or I and J the transition is $4e \leftrightarrow 2e + 2e$, corresponding to the elliptic-elliptic stability (sM). Between B and I the transition is $2e \leftrightarrow 4e + 2h$, corresponding to an elliptic-hyperbolic character (uM).

Bifurcations within a given type of \mathcal{E}_{hl} tend to be simpler because of the overall conservation of topology. The Kovalevskaya system provides (again!) four examples of fairly general scenarios:

SN: saddle-node bifurcation $\emptyset \leftrightarrow e + h$; a pair of elliptic and hyperbolic periodic orbits appears out of nothing.

ePF: elliptic pitchfork bifurcation $e \leftrightarrow h + 2e$; an elliptic orbit becomes hyperbolic and gives birth to two new elliptic orbits.

hPF: hyperbolic pitchfork bifurcation $h \leftrightarrow e + h^2$; an hyperbolic orbit turns elliptic and gives birth to two new hyperbolic orbits.

hPD: hyperbolic period doubling bifurcation $h^* \leftrightarrow e + h$; an inverse hyperbolic orbit becomes elliptic and gives birth to a hyperbolic orbit of twice the old period.

(The obvious fifth candidate in the above list, the elliptic period doubling bifurcation ePD: $e \leftrightarrow h^* + e$ does not occur in the Kovalevskaya system.)

From figure 6 and our description of the Appelrot lines it is easy to identify where in (h, l, k) space these bifurcations of critical tori are to be found.

Saddle-node bifurcations occur at the transitions $B \leftrightarrow C$ and $B \leftrightarrow J$, along the line

$$\text{SN: } l^2 = 2(2h/3)^3, \quad k^2 = 1 - h^2/3, \quad 0 < h < \sqrt{3}. \quad (48)$$

Elliptic pitchfork bifurcations occur at transitions $A \leftrightarrow B$ and $F \leftrightarrow G$, along the line

$$\text{ePF: } l^2 = 2h, \quad k^2 = 0, \quad h > 0. \quad (49)$$

In Appelrot's classification, this is the transition from class II to class III orbits.

Hyperbolic pitchfork bifurcations occur at the transition $E \leftrightarrow D$, along the line

$$\text{hPF: } l^2 = l_{\pm}^2 = h \pm \sqrt{h^2 - 2}, \quad k^2 = 1/l_{\pm}^4, \quad (50)$$

with $h > \sqrt{2}$ for $l^2 = l_-^2$ and $\sqrt{2} < h < 1.5$ for $l^2 = l_+^2$.

Hyperbolic period doubling bifurcations occur at the transition $E \leftrightarrow H$, along the line

$$\text{hPD: } l^2 = l_+^2 = h + \sqrt{h^2 - 2}, \quad k^2 = 1/l_+^4, \quad h > 1.5. \quad (51)$$

To sum up, we have analyzed three kinds of bifurcation diagrams:

- The full three-dimensional (h, l, k) bifurcation diagram where each point represents one, two, or four invariant tori T_{hlk} , depending on the Kharlamov region. The T_{hlk} are T^2 in reduced phase space T^*S^2 , and T^3 in the full phase space $T^*SO(3)$. The five Kharlamov regions i through v are separated by two-dimensional surfaces of critical values (h, l, k) , corresponding to critical tori. The critical tori come in four analytically defined Appelrot classes I through IV, or in four topologically defined types e, h, h^* , h^2 . Counting each Kharlamov region according to its multiplicity, we find $1 \times 1 + 3 \times 2 + 1 \times 4 = 11$ different families of non-critical tori (with positive values of l).
- Two-dimensional (l, k) bifurcation diagrams which are *slices* of the (h, l, k) bifurcation diagram at fixed values of the energy h . These are convenient representations of entire energy surfaces \mathcal{E}_h , of which there are eight different kinds. The critical tori form Appelrot lines. Their topological character as well as the multiplicity of tori in the Kharlamov regions is made explicit by translating lines of constant l into Fomenko graphs. These graphs may be interpreted as representations of reduced energy surfaces \mathcal{E}_{hl} . They change their character at values (h, l) where critical tori bifurcate.
- Two-dimensional (h, l) bifurcation diagrams which are *projections* onto the (h, l) plane of the lines in the (h, l, k) bifurcation diagram where critical tori bifurcate. These lines define 10 phases A ... J of reduced energy surfaces \mathcal{E}_{hl} , or Fomenko diagrams. The three lines H, U, M represent relative equilibria and mark topological changes between four kinds of \mathcal{E}_{hl} . The other four lines SN, ePF, hPF, hPD indicate standard bifurcations of critical orbits without changes of the topology of \mathcal{E}_{hl} .

The film attempts to illustrate the nature of the phases A ... J in terms of animated l -space projections of \mathcal{E}_{hl} foliations, for typical value sets (h, l) from all (h, l) phases except G and J. Tori of a continuous family are given the same color for easy identification. (Symmetry related families of tori are not distinguished by color.)

The first example is phase B with $(h, l) = (1.2, 1.58)$. The symmetric tori at $k^2 > k_{\text{sep}}^2$ are shown in red. The red family occurs for all sets of (h, l) , for sufficiently high values of k^2 . It starts with a critical torus of topological type e and Appelrot class IV at $k^2 = k_{\text{max}}^2$. At $k^2 = k_{\text{sep}}^2$ there is a critical orbit of type h. The pairs of symmetry related tori at $k^2 < k_{\text{sep}}^2$ are shown in green. The two green families exist in the neighborhood of $k^2 = 0$, for all (h, l) except phases A and F. They end in critical tori of topological type e and Appelrot class I.

The simplest phase is A, with only one type of (red) tori. Its Fomenko graph is a single edge. The film shows all tori for $(h, l^2) = (-0.5, 1)$, from $k_{\text{max}}^2 = 1.711$ (type e, Appelrot class IV) down to $k_{\text{min}}^2 = 1$ (type e, Appelrot class II). Phase B emerges from A by an elliptic pitchfork bifurcation of the critical torus at $k^2 = k_{\text{min}}^2 = 0$.

The next example is $(h, l^2) = (0.9, 0.34)$ from phase C. When k^2 is lowered from $k_{\text{max}}^2 = 2.998$, a new family of tori (blue) appears out of a saddle-node (or tangent) bifurcation at $k^2 = 0.826$. The red and blue families meet in a separatrix of type h, at

$k^2 = 0.796$, which contains an unstable critical torus, of Appelrot class IV. On the other side of the separatrix, for k values $0.796 > k^2 > 0.533$, there exists a third family of (orange) tori. It ends at $k^2 = 0.533$, in another separatrix of type h whose center is again a hyperbolic periodic orbit. For k values still lower, we recover the two symmetry related green tori. The Fomenko graph C is a convenient summary of this scenario.

The four (h, l) -phases A, B, C, J are different foliations of $\mathcal{E}_{hl} \simeq S^3$; the three phases D, E, H are different foliations of $\mathcal{E}_{hl} \simeq RP^3$; the two phases F, G are different foliations of $\mathcal{E}_{hl} \simeq S^1 \times S^2$, and phase I is only one where $\mathcal{E}_{hl} \simeq K^3$.

The transition from C to D involves a bifurcation of the energy surface \mathcal{E}_{hl} , from S^3 to RP^3 . This goes along with a different organization of tori. For the case $(h, l^2) = (1.2, 0.4)$ from phase D we start with $k_{\max}^2 = 3.901$ and see the blue family emerging at $k^2 = 1.151$, as in phase C. But the merging of red and blue tori is different: the separatrix at $k^2 = 1$ is of type h^2 and contains *two* hyperbolic orbits of Appelrot class III, out of which two symmetric yellow families of tori develop. These tori become critical again at $k^2 = 0.828$, with two independent separatrices of type h^* , each containing a hyperbolic orbit of Appelrot class IV. On the low- k side, these turn into the familiar green families.

In the transition from D to E, the blue family disappears in an hyperbolic pitchfork bifurcation: one stable and two unstable critical orbits turn into a single unstable orbit. Phase E is illustrated with $(h, l^2) = (1.85, 1.43)$. Starting at $k_{\max}^2 = 7.850$, the red family transforms directly into the two yellow families. The hyperbolic orbit at $k^2 = 1.394$ is of type h and Appelrot class IV. The transformation of yellow into green orbits at $k^2 = 0.601$ proceeds as in phase D (topological type h^* and Appelrot class IV).

In phase F, the energy surface has the topology of $S^1 \times S^2$. Except for this difference, the foliation by invariant tori is similar to that in phase B. For the example of $(h, l^2) = (2.5, 5.3)$, the film first shows the l projection of all tori, and then the physical motion corresponding to the critical tori. At $k_{\max}^2 = 15.00$, periodicity in the reduced phase space means synchrony between ψ -rotation and ϑ -oscillation; the full motion is quasiperiodic because the period of the φ -precession is incommensurate with the period of the other two angles. While this motion is stable, the separatrix at $k^2 = 0.616$ contains an unstable periodic orbit (type h and Appelrot class IV) with similar physical appearance. At $k_{\min}^2 = 0.0225$ there are two stable critical tori (type e and Appelrot class II). Their symmetry relation via S_3 , see (23), may be described as an exchange of the two weights on the axis e_3 .

The last two examples of foliations are taken from the neighborhood of the point $(h, l^2) = (h_i, l_i^2)$, see (30), where all four topological types of energy surfaces meet. With $(h, l^2) = (1.85, 3.29)$, we are close to that point in phase H. Starting at $k_{\max}^2 = 9.741$, the red family survives almost the entire range of k values, down to the separatrix of type h at $k^2 = 0.0786$, containing a critical torus of Appelrot class IV, where two yellow tori appear in a symmetry breaking bifurcation. At $k^2 = 0.0420$ these tori develop into separatrices of type h containing Appelrot orbits of class III. Each of these gives birth to two families as k^2 decreases, one violet, the other green. The violet tori end in a stable critical orbit at $k^2 = 0.0254$ whereas the green families persist down to $k^2 = 0$. (When the stable critical tori of the violet family are continued, with increasing l^2 , until $k^2 = 0$ at the transition

to phase G, they develop into the stable merry-go-round motion.)

For $(h, l^2) = (1.8, 3.26)$, we are in phase I. The energy surface K^3 derives from an accessible region in configuration space which is a sphere with three holes. This is the most complicated situations of all even though it appears only in a tiny part of parameter space. The red family extends from $k_{\max}^2 = 9.475$ down to $k^2 = 0.0289$, where a critical torus of type h and Appelrot class III gives birth to a symmetric pair of tori shown in turquoise color. These tori bifurcate again, at a separatrix with $k^2 = 0.0104$, of type h. Both pairs extend down to $k^2 = 0$ where they end in stable periodic orbits (type e, Appelrot class I).

5 Poincaré surfaces of section

5.1 General considerations

Poincaré had the idea to visualize the dynamics on three-dimensional energy surfaces in terms of well-chosen cross-sections [24]. In the case of \mathcal{E}_{hl} he would have proposed to identify a two-dimensional surface $\Sigma_{hl} \subset \mathcal{E}_{hl}$ that intersects the tori T_{hlk} in one-dimensional manifolds, either in single topological circles, or, in case of multiple intersections, in collections of circles. In a convenient representation of such a *surface of section*, essential features of the complete foliation can be observed in a single picture.

Let the Poincaré surface of section be defined by a condition $S(\mathbf{x} = 0)$,

$$\Sigma_{hl} = \{\mathbf{x} \in \mathcal{E}_{hl} \mid S(\mathbf{x} = 0)\}. \quad (52)$$

Starting the phase space flow in a point $\mathbf{x} \in \Sigma_{hl}$, and waiting for the next intersection of the corresponding trajectory with Σ_{hl} , one generates a discrete map $P : \Sigma_{hl} \rightarrow \Sigma_{hl}$, called the *Poincaré map*. Such maps were studied intensely by Birkhoff [4, 5], and played an important role in the analysis of non-integrable motion. The Moser twist theorem [22] starts from this discrete version of the phase space dynamics. The method has found wide application ever since it became possible to produce graphical renderings of Poincaré maps with the help of computers. For examples with different physical systems see the IWF films C1574 and C1654 [27, 28].

Ideally, a Poincaré surface of section should have the following properties:

1. Σ_{hl} ought to be a manifold;
2. Σ_{hl} ought to be everywhere transverse to the phase space flow;
3. Σ_{hl} ought to be Σ -complete, i. e., ensure that each point $\mathbf{x} \in \Sigma_h$ has at least one image $P(\mathbf{x})$ and one preimage $P^{-1}(\mathbf{x})$ in Σ_{hl} ;
4. Σ_{hl} ought to be \mathcal{E} -complete, i. e., ensure that every orbit in \mathcal{E}_{hl} has an intersection with Σ_{hl} .

It turns out that as a rule, not all four requirements can be met [12, 7]. However, if tangencies are accepted, it is possible to fulfill condition 1 and the two completeness conditions. A surface of section will be called *complete* if it is Σ - and \mathcal{E} -complete.

The Kovalevskaya system can be analyzed in these terms. It was shown in [9, 10] that

$$\gamma_2 = 0 \quad (53)$$

defines a complete surface of section Σ_{hl} . From the effective potential $V_{\text{eff}}(\gamma_2 = 0)$ in (40) we can identify the topological nature of Σ_{hl} , using a similar reasoning as for the identification of the four types of energy surfaces \mathcal{E}_{hl} in Section 3.2. Depending on the accessible part Q_{hl} of configuration space, the condition $\gamma_2 = 0$, reduced to the γ -sphere, gives either a circle S^1 (at high energies) or from one to three intervals D^1 . Combining these with the appropriate momentum circles, we obtain

1. $\Sigma_{lh} \simeq T^2$ where $\mathcal{E}_{hl} \simeq \mathbb{RP}^3$;
2. $\Sigma_{lh} \simeq S^2$ where $\mathcal{E}_{hl} \simeq S^3$;
3. $\Sigma_{lh} \simeq 2S^2$ where $\mathcal{E}_{hl} \simeq S^1 \times S^2$;
4. $\Sigma_{lh} \simeq 3S^2$ where $\mathcal{E}_{hl} \simeq K^3$.

The surfaces of section $\gamma_2 = 0$ are orientable manifolds with insides $\gamma_2 < 0$ and outsides $\gamma_2 > 0$. (If γ_2 were an angular variable, $\gamma_2 \in S^1$, such a statement would be meaningless. It is important that the set of γ_2 forms an interval, $\gamma_2 \in D^1$.) A trajectory that enters the inside has to come out again, and vice versa. Hence all trajectories are still captured if we record them on their way out, i.e., we impose the additional condition $\dot{\gamma}_2 \geq 0$. The surface of section Σ_{hl} is cut in two pieces (or two sets of pieces) Σ_{hl}^+ and Σ_{hl}^- along the line(s) $\dot{\gamma}_2 = 0$ of tangential flow. The part(s) Σ_{hl}^+ where $\dot{\gamma}_2 \geq 0$ may be conveniently represented in two-dimensional projection.

The conditions $\gamma_2 = 0$, $\dot{\gamma}_2 \geq 0$, are invariant under the symmetry transformation S_2 , but S_3 turns the inside out, as $\dot{\gamma}_2 \geq 0$ changes into $\dot{\gamma}_2 \leq 0$.

In terms of Euler angles, these conditions are expressed in two parts, one for $\gamma_1 > 0$, the other for $\gamma_1 < 0$:

$$\psi = \begin{cases} \pi/2 & \text{and } \dot{\psi} \leq 0 \quad (\gamma_1 > 0), \\ 3\pi/2 & \text{and } \dot{\psi} \geq 0 \quad (\gamma_1 < 0). \end{cases} \quad (54)$$

5.2 Foliations of S^3

In the film, the concept of a Poincaré surface of section is introduced and illustrated with values (h, l) from the three phases A, B, C, where $\mathcal{E}_{hl} \simeq S^3$ and $\Sigma_{hl} \simeq S^2$. To obtain a topologically fair representation of \mathcal{E}_{hl} and its foliation by invariant tori, the following procedure has been implemented.

In the first step, the accessible region of configuration space Q_{hl} is mapped to a disk $D^2(x, y)$. We know from (39) that at given (h, l) , the minimum possible value of γ_1

occurs for $\gamma_3 = 0$ and is $\gamma_1^{\min} = l^2/4 - h$. Defining the angle θ via $\gamma_1 = \cos \theta$, we have $\theta \leq \theta_{\max} < \pi$, where $\cos \theta_{\max} = \gamma_1^{\min}$. The mapping from the $\boldsymbol{\gamma}$ -disk to the (x, y) -disk is defined by

$$\begin{pmatrix} x \\ y \end{pmatrix} = \frac{\theta}{\sin \theta} \begin{pmatrix} \gamma_2 \\ \gamma_3 \end{pmatrix} =: a \begin{pmatrix} \gamma_2 \\ \gamma_3 \end{pmatrix}. \quad (55)$$

The point $\boldsymbol{\gamma} = (\cos \theta_{\max}, \sin \theta_{\max}, 0)$ is thereby mapped to $(x, y) =: (x_{\max}, 0)$.

In the second step, we attach to each point (x, y) its momentum circle from \mathbf{l} space, using the equation of motion $\dot{\boldsymbol{\gamma}} = \boldsymbol{\gamma} \times \boldsymbol{\omega}$ and the Jacobian of the mapping (55):

$$\begin{pmatrix} v_x \\ v_y \end{pmatrix} = \frac{\partial(x, y)}{\partial(\gamma_1, \gamma_2, \gamma_3)} \begin{pmatrix} \dot{\gamma}_1 \\ \dot{\gamma}_2 \\ \dot{\gamma}_3 \end{pmatrix} = \frac{a\gamma_1 - 1}{1 - \gamma_1^2} \begin{pmatrix} \gamma_2 \dot{\gamma}_1 \\ \gamma_3 \dot{\gamma}_1 \end{pmatrix} + a \begin{pmatrix} \dot{\gamma}_2 \\ \dot{\gamma}_3 \end{pmatrix}. \quad (56)$$

The set of all points $(x, y, v_x, v_y) \subset \mathbb{R}^4$ so constructed is homeomorphic to the energy surface $\mathcal{E}_{hl} \simeq S^3$.

The third step is a stereographic projection of this S^3 from its outermost point $(x, y, v_x, v_y) = (x_{\max}, 0, 0, 0)$ into $\mathbb{R}^3(Y, V_x, V_y)$ by means of the equations

$$\begin{pmatrix} Y \\ V_x \\ V_y \end{pmatrix} = \frac{1}{2} \frac{1}{x_{\max} - x} \begin{pmatrix} y \\ v_x \\ v_y \end{pmatrix}. \quad (57)$$

The point $(x_{\max}, 0, 0, 0)$ is thereby mapped to a 2-sphere at infinity. Finally, in the last step, we pull the Euclidean (Y, V_x, V_y) space into a ball of radius 2 by means of the contraction

$$r = \sqrt{Y^2 + V_x^2 + V_y^2} \quad \mapsto \quad r' = \frac{4}{\pi} \arctan r. \quad (58)$$

The result is a homeomorphic representation of \mathcal{E}_{hl} inside this ball, except that the point $(x_{\max}, 0, 0, 0)$ is represented as the surface of the ball. Its advantage as compared to the projection into \mathbf{l} space is that tori do not intersect themselves, nor do they intersect each other. The nature of the foliations becomes accessible to intuition. (We better avoid to pick out the torus which contains the point $(x_{\max}, 0, 0, 0)$.)

For (h, l) values from phase A, the situation is particularly simple. The two critical tori are two entangled circles, and as k is moved away from the critical values, the corresponding tori enclose each other.

The Poincaré surface of section Σ_{hl} is neatly seen to be intersecting all tori. Cutting away those parts of the tori which lie outside Σ_{hl} , we obtain a particularly good impression of the complete foliation.

The foliations in phases B and C are more complicated, due to the existence of further critical tori, and several families. In phase B there are an unstable and three stable critical tori. They appear to be mutually entangled, and the tori of the three families are arranged around them in a rather complicated way. Again, the main features of this arrangement are best seen by looking into the intersecting Poincaré sphere, after the exterior parts of the tori have been discarded.

In phase C, with four stable and two unstable critical tori, the foliation becomes irritatingly complex. For this reason, we gave up to try and show the last case of S^3 foliation, phase J. We also do not show examples with different types of energy surfaces. Corresponding mappings into \mathbb{R}^3 would require cutting and identification along certain surfaces which we think would overly strain the imagination.

5.3 Complete set of Poincaré surfaces of section

To simplify the picture and yet retain the essential information about the organization of tori, we turn to the last level of abstraction and restrict the view to the Poincaré surface Σ_{hl} . More precisely, we take the half Σ_{hl}^+ where trajectories leave the interior $\gamma_2 < 0$, and consider it in projection onto the $(\vartheta, \pi_\vartheta)$ plane. Since on Σ_{hl} we have $\sin \vartheta = \gamma_1$ and $\pi_\vartheta = \pm l_2 = \pm 2q$, this projection is equivalent to a (γ_1, q) projection. But note that the two pieces $\psi = \pi/2$ and $\psi = 3\pi/2$ (or $\gamma_1 > 0$ and $\gamma_1 < 0$) project to the same part of the $(\vartheta, \pi_\vartheta)$ plane. In order to have a 1:1 projection, we let ϑ vary, formally, between $-\pi/2$ and $3\pi/2$, i. e., we take $\vartheta = \arcsin \gamma_1$ if $\gamma_3 \geq 0$, and $\vartheta = \pi - \arcsin \gamma_1$ if $\gamma_3 \leq 0$. The projection so defined is continuous at $\vartheta = 0$ and $\vartheta = \pi$. It is an annulus $S^1 \times D^1$ if $\Sigma_{hl} \simeq T^2$, and one, two, or three disks D^2 if Σ_{hl} is one, two, or three 2-spheres.

Let \mathcal{P}_{hl} denote this projection of Σ_{hl} to the $(\vartheta, \pi_\vartheta)$ plane. Its boundary $\partial\mathcal{P}_{hl}$ is defined by $\dot{\gamma}_2 = 0$; with (17) this implies $p\gamma_3 = r\gamma_1$, and using the constants of motion we find

$$\partial\mathcal{P}_{hl} : \quad 2(h + \gamma_1 - q^2)(1 + \gamma_1^2) - l^2 = 0. \quad (59)$$

As h and l are fixed, this defines a boundary in the (γ_1, q) plane which is symmetric with respect to $q \mapsto -q$ (or $\pi_\vartheta \mapsto -\pi_\vartheta$) and $\vartheta \mapsto \pi - \vartheta$ (because of $\gamma_1 = \pm \sin \vartheta$, at $\gamma_2 = 0$). The completeness of the surface of section implies that topological changes of the energy surfaces \mathcal{E}_{hl} are reflected in topological changes of $\partial\mathcal{P}_{hl}$. It is empty for $h < l^2/4$ and turns into a circle as h increases beyond $l^2/4$ (sleeping top in hanging position). The transition associated with the sleeping top in upright position occurs when $\partial\mathcal{P}_{hl}$ reaches the point $(\gamma_1, q) = (-1, 0)$. The merry-go-round motion can be obtained from a consideration of the number of zeroes of the polynomial (59) on the line $q = 0$; the same polynomial was discussed in Eqs. (41) and (42).

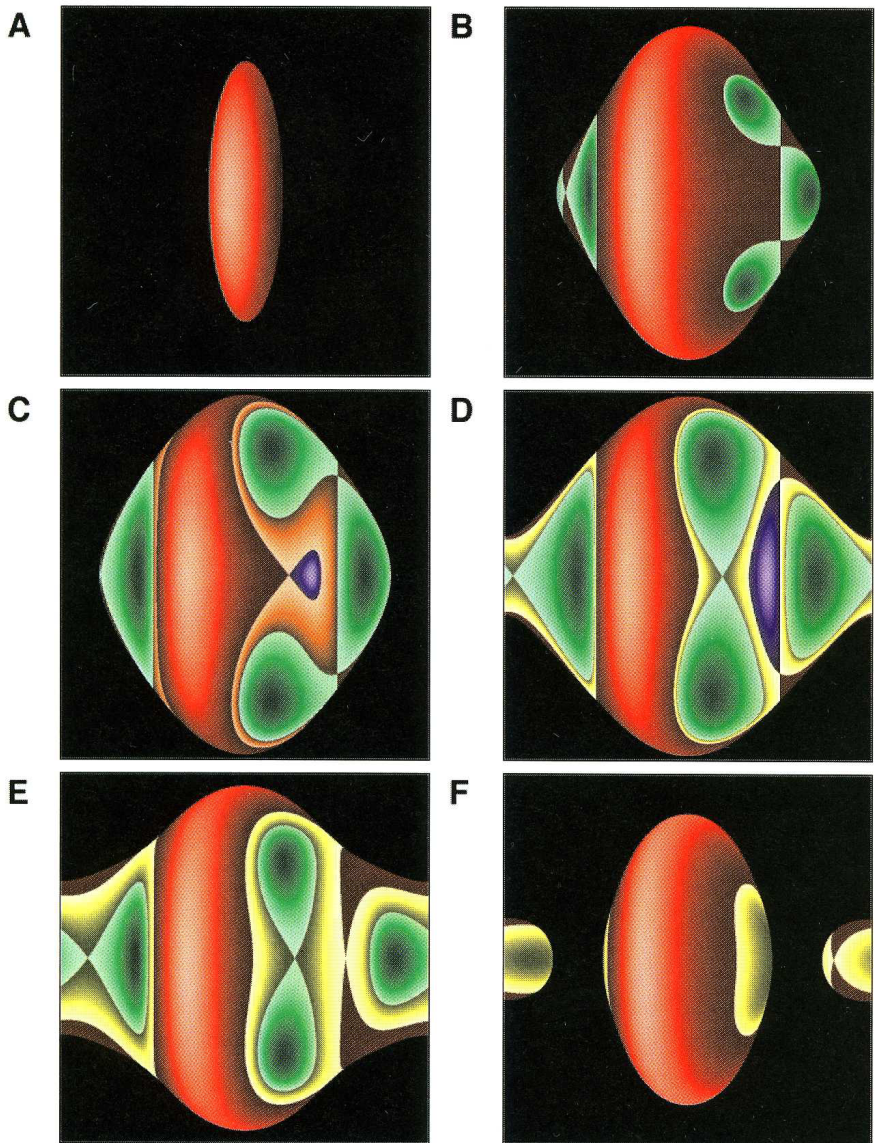


Fig. 9a: Typical Poincaré surfaces \mathcal{P}_{hl} for the six (h, l) -phases A ... F as defined in Figure 4. The invariant tori are given as level lines of equal color. The abscissa ϑ ranges from $-\pi/2$ to $3\pi/2$ in each picture; the units of the ordinate π_ϑ depend on (h, l^2) which are as follows:
 A: $(-0.5, 1)$ B: $(1.2, 1.58)$ C: $(0.9, 0.34)$ D: $(1.2, 0.4)$ E: $(1.85, 1.43)$ F: $(2.5, 5.3)$

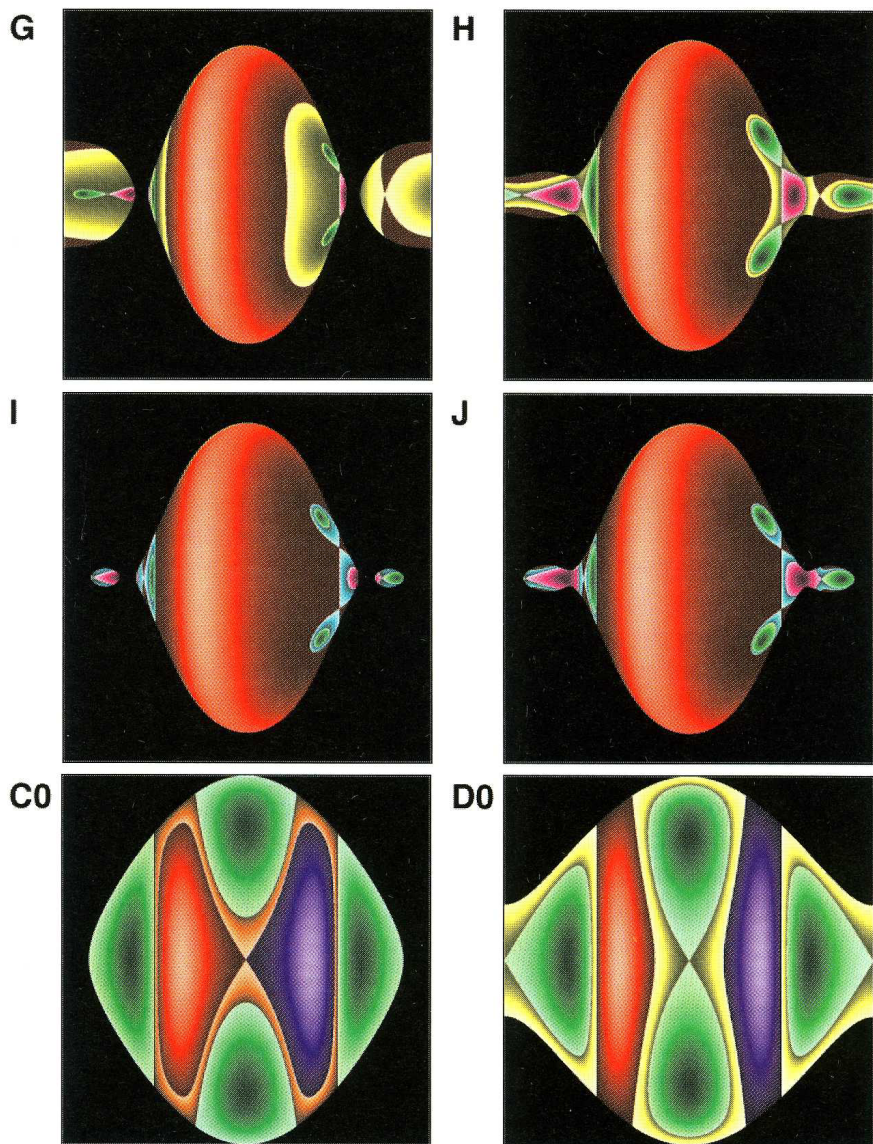


Fig. 9b: Poincaré surfaces \mathcal{P}_{hl} for the (h, l) -phases G, H, I, J, and two examples from C and D with $l = 0$. From top left to bottom right:
 G: (2.5, 4.82) H: (1.85, 3.29) I: (1.8, 3.26) J: (1.8, 3.23) C0: (0.9, 0)
 D0:(1.2, 0).

The film displays Poincaré surfaces \mathcal{P}_{hl} in continuous coloring, see Figure 9. Each family of tori is given a basic color (red, orange, blue, yellow, green, turquoise, violet). Within a given family, the value of the Kovalevskaya constant is indicated by brightness: dark for low k^2 , light for high k^2 . Stable critical tori can be recognized as dark and light centers, separatrices show up as color discontinuities. Unstable critical tori appear as intersections of these discontinuities.

In [9] it was shown how the contour lines of constant k^2 can be obtained as integral curves of an appropriately constructed two-dimensional flow. The complete analysis of Appelrot classes and their bifurcations may be given in terms of the behavior of critical points of this flow. The results collected in Section 4 were obtained with this method.

If \mathcal{P}_{hl} gives an idea of how the reduced energy surface \mathcal{E}_{hl} is foliated by tori, then a picture of the complete energy surface \mathcal{E}_h is obtained by varying l^2 from zero to its maximum value at fixed h , $l_{\max}^2 = 4(h+1)$. (Positive and negative l give symmetric pictures.) The film does this in a continuous manner, showing animated sequences for four values of energy h . In the first case, $h = -0.2$, there exists only one family of tori, the red ones. The reduced energy surfaces \mathcal{E}_{hl} are 3-spheres S^3 , the surfaces of section Σ_{hl} are 2-spheres S^2 , and their projections \mathcal{P}_{hl} are disks D^2 , see Figure 9A. With increasing l^2 , the disk shrinks to a point, corresponding to the critical torus where the top sleeps in hanging position.

The second series shows the case $h = 1.2$. At low values of l^2 , the reduced energy surface $\mathcal{E}_{hl} \simeq \mathbb{RP}^3$, the Poincaré surface $\Sigma_{hl} \simeq T^2$, and its projection \mathcal{P}_{hl} is an annulus $D^1 \times S^1$. Figures 9D0 and 9D are taken from this part of the animation. As l^2 increases beyond $4(h-1)$, \mathcal{E}_{hl} changes into S^3 , and the yellow tori disappear. At the point of transition, they develop into a separatrix which contains three hyperbolic periodic orbits: one of them the sleeping top in upright position, the other two sitting in the border between red, blue and green regions (there are neither yellow nor orange tori at the transition point). With l^2 growing further, we see foliations of types C, B, A.

A few comments are in order about the relationship between the families of tori involved. The red and blue families are images of each other under time reversal. They appear as a symmetric pair at $l = 0$, and to each \mathcal{P}_{hl} there corresponds a picture of $\mathcal{P}_{h,-l}$ where (i) blue and red are interchanged, (ii) the coordinates are inverted at the center (note that the condition $\dot{\gamma}_2 > 0$ changes sign under time reversal). As long as blue and red tori coexist, for given l^2 , they share a range of k^2 -values. For k^2 greater than the maximum value in the blue family, the red family continues smoothly. For k^2 smaller than the minimum value in the blue family, the red tori cease to exist, and orange takes over. The distinction between red and orange tori vanishes at the tangent bifurcation from region C to region B; thus red and orange tori have the same symmetry properties, yet in phase C they are held apart by a separatrix. In phase B, see Figure 9B, there are four dark green centers, hence it appears as if there are four green tori rather than two. This is not the case; each of the two green tori has two intersections with \mathcal{P}_{hl} , the Poincaré map at the green centers has period two. (The centers on the γ_1 axis belong to the same orbit.)³

³When an orbit develops a little loop in phase space, this may induce a period doubling of the Poincaré

The third series, $h = 2.5$, is representative for high energies. The sequence of reduced energy surfaces is $\mathcal{E}_{hl} \simeq \mathbb{RP}^3$, then $\mathcal{E}_{hl} \simeq S^1 \times S^2$, and finally $\mathcal{E}_{hl} \simeq S^3$. The Poincaré surfaces of section Σ_{hl} are, respectively, 2-tori, then two 2-spheres, then a single 2-sphere. The corresponding projections \mathcal{P}_{hl} are an annulus (in phases D, E, H), then two disks (in phases G, F), then a single disk (in phase A). In the transition from D to E, the blue tori disappear in an hyperbolic pitchfork bifurcation: a stable and two unstable critical orbits combine to a single unstable orbit, at the center of a separatrix between yellow and red. The transition from E to H is of a different kind. It involves a period doubling of the two inverse hyperbolic periodic orbits in the separatrix between green and yellow; they each develop into a stable center (violet) and a normal hyperbolic orbit with twice the original period, and two intersections with the Poincaré surface (transition $h^* \rightarrow e + h$.) Between H and G, cf. Figure 9H and 9G, the projection \mathcal{P}_{hl} decays into two disks, reflecting the change of topology of \mathcal{E}_{hl} . The point of disruption is the center of the violet phase; it corresponds to the stable merry-go-round motion. Between G and F there is an elliptic pitchfork bifurcation: two stable critical orbits (one violet, the other green) merge to become the stable center of a yellow region. (Remember: two green centers in the Poincaré section belong to the same orbit.) Finally, in the transition from F to A, the topology of Σ_{hl} changes from two 2-spheres to one 2-sphere; the upright sleeping top disappears together with the yellow tori. As may be inferred from Figure 9F, the small component of \mathcal{P}_{hl} near $\gamma_1 = -1$ contains a stable and an unstable critical orbit. This accounts for the elliptic-hyperbolic character of the relative equilibrium along the bifurcation line between F and A, in contrast to the hyperbolic-hyperbolic character of the same relative equilibrium along the line between D and C, see Figure 9D, or between H and J, see Figure 9H.

The last series is taken at $h = 1.75$, with a small range of l^2 that comprises regions H, J, I, and B. The energy surface changes at every transition, from \mathbb{RP}^3 to S^3 to K^3 to S^3 . In the transition from H to J there is a constriction at the point $\gamma_1 = -1$. In a similar way as we observed the transition from yellow to orange tori between D and C, there is now a crossover from yellow to turquoise orbits; neither of them exists right at the transition point. Going from J to I, there is a constriction right at the centers of the two violet regions – the stable merry-go-round motion. When the two small disks of phase I degenerate to two points, in the transition to B, the unstable (elliptic-hyperbolic) merry-go-round equilibrium appears. At slightly larger l^2 , the violet and green tori of phase I have disappeared, and the turquoise tori from phase I have turned green in B, in a similar way as the orange tori turn red in the transition from C to B.

map even though the orbit does not bifurcate in phase space. *True* period doubling as in $e \rightarrow h+e$ involves a doubling of the *time* it takes to traverse the elliptic orbit. What we see in a comparison of Poincaré sections A and B is a pitchfork bifurcation $e(\text{red}) \rightarrow h+2e(\text{green})$, accompanied by (an accidental) period doubling of the Poincaré map.

6 Back to the top

We have come to a fairly high level of abstraction in the analysis of the Kovalevskaya top. In contrast to the classical interest of *rational mechanics* in the behavior of single trajectories, our focus has been on the geometry of phase space, with the aim of getting a complete survey on all possible physical motions, and on the way in which these are organized in phase space.

The Kovalevskaya top is an integrable system with three degrees of freedom. Hence its natural phase space $T^*SO(3)$ has six dimensions. Its five-dimensional energy surfaces \mathcal{E}_h are foliated by three-dimensional Liouville-Arnold tori. One degree of freedom (the φ motion) can be separated, leaving us with a reduced system of two degrees of freedom, three-dimensional energy surfaces \mathcal{E}_{hl} , and their foliation by two-dimensional invariant tori. It is convenient to embed this reduced description in another six-dimensional phase space P_l , equipped with a Poisson structure \mathbf{J}_p and two Casimir constants. The equations of motion are then the familiar Euler-Poisson equations plus an extra equation for φ . (In practice, as noted in the introduction, it is preferable to work with an eight-dimensional phase space $T^*\mathbb{R}^4$ where \mathbb{R}^4 is understood to be the embedding space for S^3 , and is equipped with the quaternion structure.)

The Casimir constant $C_\gamma = 1$ defines a unit 2-sphere in γ space, and for each γ , the other constant $C_l = l$ defines a 2-plane in l space. This gives the reduced phase space the structure of $S^2 \times \mathbb{R}^2$. The corresponding invariant tori are defined by the values h of energy and k^2 of the Kovalevskaya constant. Their most direct representation is in terms of projections onto the γ sphere and into l space. We looked at animated sequences of such projections at fixed (h, l) , varying the values of k^2 through the allowed range. This revealed a startling complexity, even of single invariant tori. To avoid the problem of projection-induced self-intersections, we turned to a homeomorphic three-dimensional representation of \mathcal{E}_{hl} , for three (h, l) values where $\mathcal{E}_{hl} \simeq S^3$, and displayed the corresponding types of foliation (A, B, C). We did not try to produce comparable renderings of the three other topological types of reduced energy surfaces.

In a last step, in order to reduce complexity and obtain a pictorial survey on the essential features of the foliations, we adopted the technique of complete Poincaré sections, where each torus is represented with one or several cross sections. Depending on (h, l) , we found ten different types of these graphs, as shown in Figure 9. Each of them gives a fair picture of the corresponding \mathcal{E}_{hl} . To get an impression of a non-reduced energy surface \mathcal{E}_h , the angular momentum l must be varied at given h . This was done in the final animation sequences where we presented four out of eight different types.

The analysis could be carried a step further by introducing action variables and representing each torus \mathcal{T}_{hlk} by the triple (I_1, I_2, I_3) of its three actions, and hence by a point in I space. A given energy surface \mathcal{E}_h can then be represented as a two-dimensional surface $h = \text{const}$ in action space. Indeed, this was done in [10], but the scope of the film did not allow us to enter this ultimate level of abstraction.

So what have we achieved? The material presented should be viewed as part of a software package available on a graphical workstation. Starting with the bifurcation

diagram Figure 4, a pair of values (h, l^2) may be selected by mouse-click. The program then displays the Poincaré section \mathcal{P}_{hl} . At a single glance, we recognize which families of tori are present. With another mouse-click, we may select any one of them and let the computer integrate the equations of motion for a corresponding trajectory. This may then be shown in whatever version we wish – in γ or l projection, or even as motion of a realistic model in “real” time. All possible motions of the Kovalevskaya system can be generated in this way, and a lot of familiarity with it may be gained by playing this game. At a time where computer power for numerical integration is available in abundance, we feel that the analysis of single trajectories in terms of hyperelliptic functions can no longer be the point. The challenge lies in the determination of invariant structures, and in their comprehensive display for easy access.

Acknowledgements

We acknowledge gratefully that we have benefitted considerably from discussions with E. Horozov, M. P. Kharlamov, M. Juhnke, I. N. Gashenenko, A. V. Bolsinov, and A. T. Fomenko.

This work was supported by a grant from the Deutsche Forschungsgemeinschaft.

References

- [1] G. G. Appel'rot. Not entirely symmetrical heavy gyroscopes (in Russian). In *Rigid Body Motion About a Fixed Point, Collection of papers in memory of S. V. Kovalevskaya*, pages 61–155. Acad. Sci. USSR, Dept. of Technical Sciences, Moscow, Leningrad, 1940.
- [2] V. I. Arnold. *Mathematical Methods of Classical Mechanics*, volume 60 of *Graduate Texts in Mathematics*. Springer, Berlin, 1978.
- [3] M. Audin. *Spinning Tops*. Cambridge University Press, Cambridge, 1996.
- [4] G. D. Birkhoff. Dynamical systems with two degrees of freedom. *Trans. Am. Math. Soc.*, 18:199–300, 1917.
- [5] G. D. Birkhoff. Surface transformations and their dynamical application. *Acta Math*, 43:1–119, 1922.
- [6] A. I. Bobenko, A. G. Reyman, and M. A. Semenov Tian Shansky. The Kowalewski top 99 years later: A Lax pair, generalizations and explicit solutions. *Commun. Math. Phys.*, 122:321–354, 1989.
- [7] A. Bolsinov, H. R. Dullin, and A. Wittek. Topology of energy surfaces and existence of transversal Poincaré sections. *J. Phys. A*, 29:4977–4985, 1996.

- [8] B. A. Dubrovin, J. M. Krichever, and S. P. Novikov. Integrable systems. I. In V. I. Arnold and S. P. Novikov, editors, *Dynamical Systems IV*, volume 4 of *Encyclopaedia of Mathematical Sciences*. Springer, New York, 1988.
- [9] H. R. Dullin. *Die Energieflächen des Kowalewskaja-Kreisels*. Mainz Verlag, Aachen, 1994.
- [10] H. R. Dullin, M. Juhnke, and P. H. Richter. Action integrals and energy surfaces of the Kovalevskaya top. *Int. J. Bifurcation and Chaos*, 4(6):1535–1562, 1994.
- [11] H. R. Dullin and A. Wittek. Efficient calculation of actions. *J. Phys. A*, 27:7461–7474, 1994.
- [12] H. R. Dullin and A. Wittek. Complete Poincaré sections and tangent sets. *J. Phys. A*, 28:7157–7180, 1995.
- [13] A. T. Fomenko. Topological classification of all integrable Hamiltonian differential equations of general type with two degrees of freedom. In T. Ratiu, editor, *The Geometry of Hamiltonian Systems*, pages 131–339, New York, 1991. Springer.
- [14] L. Haine and E. Horozov. A Lax pair for Kowalewski’s top. *Physica*, 29D:173–180, 1987.
- [15] E. Horozov and P. van Moerbeke. The full geometry of Kowalewski’s top and (1,2)-Abelian surfaces. *Commun. Pure Appl. Math.*, 42:357–407, 1989.
- [16] M. P. Kharlamov. Bifurcation of common levels of first integrals of the Kovalevskaya problem. *Prikl. Matem. Mekhan.*, 47(6):737–743, 1983.
- [17] F. Klein and A. Sommerfeld. *Über die Theorie des Kreisels*. Teubner, Leipzig, 1910.
- [18] F. Kötter. Sur le cas traité par Mme Kowalevski de rotation d’un corps solide autour d’un point fixe. *Acta Math.*, 17:209–264, 1893.
- [19] S. Kowalevski. Sur le problème de la rotation d’un corps solide d’un point fixe. *Acta Math.*, 12:177–232, 1889.
- [20] S. Kowalevski. Sur une propriété du système d’équations différentielles qui définit la rotation d’un corps solide d’un point fixe. *Acta Math.*, 14:81–93, 1889.
- [21] D. Lewis, T. Ratiu, J. C. Simo, and J. E. Marsden. The heavy top: a geometric treatment. *Nonlinearity*, 5:1–48, 1992.
- [22] J. Moser. On invariant curves of area-preserving mappings of an annulus. *Nachr. Akad. Wiss. Göttingen, Math. Phys. Kl. IIa*, (1):1–20, 1962.
- [23] A. A. Oshemkov. Fomenko invariants for the main integrable cases of the rigid body motion equations. In A. T. Fomenko, editor, *Topological Classification of Integrable Systems*, pages 67–146, Providence, RI, 1991. American Mathematical Society.

- [24] H. Poincaré. *Les Méthodes Nouvelles de la Mécanique Céleste*. Gauthier-Villars, Paris, 1892. Translated by the AIP, History of Modern Physics and Astronomy, Vol. 13, (1993).
- [25] P. H. Richter, H. R. Dullin, H. Waalkens, and J. Wiersig. Spherical pendulum, actions and spin. *J. Phys. Chem.*, 100:19 124–19 135, 1996.
- [26] P. H. Richter, H. R. Dullin, and A. Wittek. *Dynamics of the Spinning Top*. Springer Verlag, Berlin, Heidelberg, New York, 1998.
- [27] P. H. Richter and H.-J. Scholz. Das ebene Doppelpendel – the planar double pendulum. *Publikationen zu Wissenschaftlichen Filmen, Sektion Technische Wissenschaften/Naturwissenschaften*, Serie 9(7):3–35, 1986. Film C1574, Institut für den Wissenschaftlichen Film (IWF), Göttingen.
- [28] P. H. Richter and H.-J. Scholz. Das eingeschränkte Dreikörperproblem – The restricted three body problem. Technical report, Institut für den Wissenschaftlichen Film (IWF), Göttingen, 1987. Film C1654.
- [29] Steven Smale. Topology and mechanics I+II. *Inv. Math.*, 10+11:305–331 + 45–64, 1970.
- [30] N. E. Zhukovsky. Geometric interpretation of the case considered by Kovalevskaya of the motion of a heavy rigid body about a fixed point. *Mat. Sbornik*, 19:45–93, 1896.